Quantized Constant-Q Gabor Atoms for Sparse Binary Representations of Cyber-Physical Signatures

Milton A. Garces[1,2]*

[1] Infrasound Laboratory, University of Hawaii, Manoa; milton@isla.hawaii.edu
[2] RedVox, Inc.; milton@redvoxsound.com
* Correspondence: milton@isla.hawaii.edu

Abstract: Increased data acquisition by uncalibrated, heterogeneous digital sensor systems such as smartphones present new challenges. Binary metrics are proposed for the quantification of cyber-physical signal characteristics and features, and a standardized constant-Q variation of the Gabor atom is developed for use with wavelet transforms. Two different continuous wavelet transform (CWT) reconstruction formulas are presented and tested under different signal-to-noise ratio (SNR) conditions. A sparse superposition of Nth order Gabor atoms worked well against a blast synthetic using the wavelet entropy and an entropy-like parametrization of the SNR as the CWT coefficient-weighting functions. The proposed methods should be well suited for sparse feature extraction and dictionary-based machine learning.

Keywords: Gabor atoms; wavelet entropy; binary metrics; acoustics; quantum wavelet

1. Introduction

This paper applies the constant-Q standardized Infrasonic Energy, Nth Octave (Inferno) framework [1] to the Gabor wavelet [2] and proposes binary metrics for signature characterization. One of the primary motivations of this work is to facilitate the fusion of multi-modal data streams in sensor systems that collect information at different temporal and spatial granularities. Consider a cyber-physical sensor system that converts observables into digital time series data consisting of a combination of signals and noise. Signals of interest can be hypothetically described by sparse representations that define their signature. If signature characteristics are sufficiently unique and recognizable from those of ambient coherent and incoherent noise, it can be used to identify and classify an object or process.

The transformation of diverse digital measurements into robust, scalable, and transportable representations is a prerequisite for signal detection, source localization, and machine learning applications for signature classification. The challenge at hand is to construct sparse signal representations that contain sufficient information for classification. Unambiguous classification can be elusive; measurement artifacts, unexpected signal variability, and non-stationary noise often conspire to add uncertainty to our classifiers. As will be discussed in this paper, information and uncertainty quantification can be substantially simplified when using standardized wavelets and binary metrics.

1.1. Binary Representations of Time and Frequency

Oscillatory processes often exhibit spatial and temporal scalability and self-similarity. Although some physical processes scale linearly, many exhibit recurrent patterns that scale logarithmically and are well represented by power laws. Both linear and logarithmic scales can coexist. For example, overtones

in harmonic acoustic systems are often linearly spaced in frequency, yet our sense of tone similarity is close to base 2 logarithmic (binary) octave scales. The term octave comes from the eight major notes in 12-tone musical notation, which closely repeat in with factors of two. This paper uses the term octave and binary interchangeably to denote the base 2 geometric scaling of frequency and time. The mapping between frequency (or pitch) and time (period) is direct for continuous tones, such as musical notes, or statistically stationary oscillations like the orbits of planets. Discrete Fourier transform methods are exceptionally well suited for the interpretation of steady tonal signals with linearly spaced harmonics. The Fourier transform deconstructs oscillations with distinct recurrent time periods into a *spectral* representation consisting of a set of discrete frequencies. The spectral transformation can be sparse because it removes time as a variable, facilitating the reconstruction of stable oscillations from a subset of coefficients in the Fourier spectrum.

Stable oscillators can be even more succinctly represented by a fundamental frequency *or* period (exclusive *or*, as they are not independent). For many physical systems, a map can be constructed between the fundamental frequency and its harmonics. Signals where the fundamental and its harmonics (when they exist) are statistically stationary and easily discernible above noise can be referred to as the easy *continuous wave* (CW) problem, or the zeroth (trivial) class of CW problems. The trivial CW problem is well understood and should routinely be used as a speed and performance benchmark for detection and classification algorithms.

The plot thickens when temporal variability is introduced in the signal or the noise. In the first class of CW problems, temporal variability is due to non-stationary broadband or band-limited noise. This is a chronic condition in infrasonic signal processing, where ambient noise can be coherent or incoherent across a dense sensor network [3] or an array aperture [4]. The first class of CW problems is also well understood when noise is predictable (e.g. normally distributed) over a time duration that is much longer or much shorter than the signal period in the detection band. However, this class of problems is not as well characterized when noise is not evenly distributed across the signal detection bandpass, and can be particularly inconvenient when noise overwhelms the fundamental frequency band.

In the second class of CW problems, temporal variability is introduced by a change in the temporal, spectral, and/or statistical properties of the signal. These changes can be due to aging, failure, motion, communication, or any other change in state. In a simple two-state problem, one may quantify the properties of the first state, the transition period between states, and the properties on the final state. In a multiple-state problem, such as with communication systems, speech, or music, the short-term discrete Fourier transform (STFT) is often used to characterize spectral variability.

If the transition period between states is faster that the characteristic time scale of the initial state, the STFT does not always provide an accurate representation of this *transient*. For some signals, the details of the transient are not relevant and only the steady states are important. But a new class of signals emerges when the detection of transient anomalies is prioritized.

The zeroth class of transient problems consist of delta functions with their integrals and derivatives. Such instantaneous spikes do not exist in the natural world but can be readily constructed digitally to evaluate the impulse response of a system or represent a neuromorphic network [5-6]. The first class of transient problems would consist of realistic variants of the delta function that may be observed in the wild when a rapid change of state becomes the signal of interest. Just like a single-tone sinusoid may be regarded as the prototype end member for the trivial CW problem, an explosive detonation could be considered as a prototype transient signal source [7]. During an explosion, observations would vary from ambient noise to a brief blast transient that fades back to a possibly perturbed ambient noise state. If the observations were acoustic at some distance from the source, the system would go from quiescence to blast to quiescence, and the transition can be devastatingly fast. In general, poorly-conditioned STFTs provides inadequate representations of brief, rapidly changing signals because the signatures no longer resemble a CW, and so are not well represented by sinusoids. However, since a STFT is a windowed

89   sinusoid, a well-conditioned STFT window at the peak frequency of a signal turns the waveform into a
90   wavelet.
91   The concept of a windowed sinusoid to represent a transient signal was introduced by Gabor (1946),
92   and later mathematically formalized by others as wavelets. Variants of the Gabor wavelet are presented
93   in the main text and the Appendices.
94   The second class of transient problems overlaps with the second class of CW problems. It
95   corresponds to transients of significant durations which could be addressed with STFTs, wavelets, or
96   their combination. Very often a transient is imbedded in a noise field with band-limited harmonic
97   structure. Or the transient itself is a sweep, characterized by a substantial frequency change in the
98   fundamental frequency and its harmonic structure.
99   The primary differences between STFTs and wavelet transform approaches are that the former uses
100 a linear period mapping and a constant processing window duration, while the latter uses geometric
101 pseudo-period mapping and a window duration that scales with the pseudo-period. Whereas in the
102 Fourier framework there is a one-to-one mapping between time and frequency, the wavelet mapping
103 between time scale and frequency can be less evident and depends on the selected wavelet.
104   This paper concentrates on developing highly standardized Gabor atoms [2] for the design and
105 evaluation of transportable, sensor-agnostic signal detection, sparse feature extraction, and classification
106 algorithms.

107 **1.2. Binary Representations of Energy and Information in Cyber-Physical Systems**

108   A Cyber-Physical System (CPS) is an algorithm-controlled computer system with physical inputs
109 and outputs. A typical example of a mobile CPS is a smartphone with a microphone input (sound
110 activation) that outputs a response (speech, music, or signal recognition) to a screen. Cyber-physical
111 Measurement and Signature Intelligence (MASINT) is an emerging discipline that concentrates on
112 phenomena transmitted through cyber-physical devices and their interconnected data networks. For
113 smartphones and other multi-sensor mobile platforms connected to wireless networks, this includes
114 digital noise, bit errors, and latencies internal to the device and its communication channels [8-10].
115   Data processed by the cyber part of CPSs are digital and represented as binary digits (bits). Although
116 the precision of the data would be initially defined by its their allocated integer word size (16, 24 bit, etc.),
117 the original data may be converted into floating point equivalents when an algorithms acts on it. For
118 example, consider sound recorded by a smartphone at the standard rate of 48,000 samples per second. A
119 typical sound record may have 16-bit resolution, so that its dynamic range in bits is 2^{-15} to $2^{15}-1$. However,
120 one may only be interested in the lower frequency components of the raw data, so one would implement
121 a lowpass anti-aliasing filter before decimation. Such filters often require floating point arithmetic in
122 double precision (52 bit mantissa re IEEE 754 at the time of this writing) to reduce instability. Therefore,
123 the precision of the resulting lowpass filtered data would exceed the specification of the original 16-bit
124 integral input. However, the theoretical dynamic range of the system would not exceed the specification
125 of the integer 16 physical input. Furthermore, data compression can be more efficient on floats than
126 integers, which leads us to the topic of fractional bits as a measure of CPS amplitude, power, and
127 information.
128   Many of the metrics we used in traditional physical and geophysical systems are inherited from the
129 analog era. The base 10 decibel scale is a measure of power relative to a reference level, and is used
130 extensively in telecommunications, acoustics, and electrical engineering. Let's estimate the hypothetical
131 dynamic range of a 16-bit microphone record of a sinusoid at full scale. The peak rms amplitude would
132 be

133
$$p_{rms\ signal} = \frac{2^{16}}{2\sqrt{2}} \ . \tag{1}$$

134   All systems have quantization and system noise, and the noise can have a positive or negative bias.
135 This is not a noise paper; for the sake of illustration, I model the system noise as oscillating around a
136 mean of zero and alternating between -1 and 1,

$$p_{rms\,noise} = \frac{2^1}{2\sqrt{2}} \;. \tag{2}$$

138 The theoretical dynamic range of the system in dB for a sinusoid recorded with a 16-bit microphone and
139 sound card combination with a one-bit noise floor could be characterized by the ratio of the power

$$10 * log_{10}\left[\frac{p_{rms\,signal}}{p_{rms\,noise}}\right]^2 = 20 * log_{10}[2^{15}] \approx 90 dB \tag{3}$$

141 where a digital response is converted to the legacy base 10 logarithmic system. One advantage of the
142 decibel approach is that it can be compared to the response of the human ear and other analog systems.
143 However, analog comparisons are not necessary for many cyber physical applications. A more natural
144 unit for CPS is the binary logarithm

$$log_2\left[\frac{p_{rms\,signal}}{p_{rms\,noise}}\right] = log_2[2^{15}] \approx 15.0 \; fbits \tag{4}$$

146 where the unit *fbits* corresponds to floating point representation of bits. For example, in 24-bit systems,
147 present-day quantization error is ~3 bits, leading to an effective dynamic range of ~21 fbits. Likewise, a
148 24-bit integer cast into a 32-bit symbol can have 8+3 bits of noise, and may be converted to a float that
149 still has ~21 fbits of dynamic range.
150   Another unit that is often specified is the ½ power point of the frequency response of a filter, which
151 defines the quality factor of that filter. This is often referred to as the -3dB point, since $10 * log_{10}(2) \sim 3dB$.
152 However, accurate filter bank reproductions require a clear specification of the ½ power point, and
153 conversion from base 10 to base 2 specification can lead to computational errors. Plotting filter responses
154 in floating point bits can be informative as it reveals the precision of the computation. Because it is
155 awkward and there is already a precedent in information theory for using bits outside of their original
156 definition as a binary digit, from here onwards in this paper the word bits will be used to represent either
157 the floating point equivalent of bits or as a metric for information.
158   Consider the communication channel capacity introduced by Shannon [11], which in its simplest
159 form can be expressed as

$$Ch = W log_2\left(\frac{Sg+Ns}{Ns}\right) \tag{5}$$

161 where Ch is a measure of the differential entropy of a signal in the presence of noise, W is a measure of
162 the bandwidth, Sg is representative of the power of a signal, and *Ns* is representative of the noise power.
163 The units of the channel capacity are in shannons, or bits per second, and represent the theoretical upper
164 bound of the rate of information transfer in a communication channel. Since it is often impossible to
165 separate noise embedded in a signal but it is often possible to construct a noise model, we can think the
166 ratio *(Sg+Ns)/Ns* as a practical measure of the signal to noise ratio (SNR) of an observed signal that has
167 been carried through a cyber-physical system or a medium.
168   The effective SNR and therefore the detectability of a compressed pulse (such as a wavelet) is the
169 product of the bandwidth, the signal to noise ratio, and the duration of a signal T [12]. When using
170 constant-Q Gabor wavelet with fractional octave (binary) bands n of order N and center frequency f_n to
171 process a signal in the presence of noise, the next section shows that for

$$SNR_n = \frac{Ns_n+Sg_n}{Ns_n} = 1 + \frac{Sg_n}{Ns_n} \tag{6}$$

173 the signal detectability per band can be represented by

$$bSNR_n = \frac{1}{2} \; log_2(SNR_n) \tag{7}$$

175 and the upper limit on rate of information in bits per second for a band-limited pulse with center
176 frequency f_n can be estimated from

$$Ch_n = \frac{f_n}{N} \, bSNR_n \qquad (8)$$

178 Energy and Shannon entropies using the binary log are constructed for both the wavelet coefficients
179 and SNR in Section 2.5.

2. Methods

181 This is an algorithmic paper providing foundational methods to construct standardized Gabor
182 wavelets within a binary framework. No materials are included or required; all the algorithms required
183 to reproduce the results are included, with recommendations for specific existing functions in open-
184 source software frameworks.
185 Although the methods are intended to be sensor-agnostic and transportable across diverse domains,
186 the selection of the Gabor mother wavelet does define the optimal applicability of the algorithms: the
187 methods in this paper will work best with a transient, or a portion of a transient, that can be well
188 represented by a superposition of Gabor wavelets. Fortunately, this covers a fairly wide range of transient
189 signature types. Furthermore, the fundamental principles in this work are expandable to other wavelets
190 as well as to four-dimensional spatiotemporal representations.

2.1. Transforming Time and Frequency to Scale

192 A digital time series is constructed by collecting digital measurements at discrete times separated
193 by a nominal sample interval $\Delta\tau_s$. One may estimate a standard deviation from nominal σ_{τ_s} associated
194 with the sample interval; when this error is a very small percent of the sample interval (e.g. parts per
195 million) it is generally treated as a constant. Some variability in the sample rate should be expected in
196 cyber-physical sensing systems under different conditions (temperature, battery level, power load, data
197 throughput, etc.) even when the systems have the same hardware configurations. This can have an
198 impact when attempting high-accuracy time synchronization. If adequate performance metrics are
199 collected, the sample rate error can be quantified and potentially compensated by an additional time-
200 varying correction to the clock drift.
201 In many scientific domains, such as astronomy and climatology, the sample interval may be greater
202 than one second. Domains where the phenomena of interest change more rapidly use the equivalent
203 metric of samples per second, referred to as the sample rate and often expressed in units of Hertz. The
204 relationship between the sample interval $\Delta\tau_s$ and its standard deviation σ_{τ_s} and the sample rate f_s
205 and its associated error can be expressed as

$$\frac{1}{\Delta\tau_s + \sigma_{\tau_s}} = \frac{1}{\Delta\tau_s}\left(1 + \frac{\sigma_{\tau_s}}{\Delta\tau_s}\right)^{-1} \approx f_s\left(1 - \frac{\sigma_{\tau_s}}{\Delta\tau_s}\right) \text{ if } \frac{\sigma_{\tau_s}}{\Delta\tau_s} \ll 1. \qquad (9)$$

207 Although time is the primary discrete sampling parameter, system requirements are often provided
208 as frequency specifications within the context of Fourier transforms. The nominal sample rate sets the
209 maximum upper edge of the bandpass of the system; there should be negligible energy at the Nyquist
210 frequency, which is half of the sample rate. The actual bandpass of a system is set by the low- and high-
211 frequency cutoffs of a cyber-physical system, which may include the sensor response, hardware
212 specifications, firmware and software modifications (such as anti-aliasing filtering), and data
213 compression.
214 The mapping between frequency and period is simple for continuous wave tone; the tone period is
215 the inverse of the tone frequency. It is not so clear for transients. Following [7], a transient with a single
216 spectral peak at a center frequency f_n may be associated with a pseudo-period $\tau_n = 1/f_n$. This mapping
217 is important as the scale of wavelet representations is linearly proportional to the pseudo-period, which

218   is also referred to as the scale period. A high-level overview of the Appendixes is provided in this section
219   for ease of reference.
220   Constant quality factor (Q) bands with constant proportional bandwidth are traditionally defined as
221   [1]

222
$$\frac{\Delta f}{f_n} = \frac{1}{Q} \tag{10}$$

223   where Δf is the bandwidth centered on f_n. The Q is a measure of the number of cycles needed to reach
224   the ½ power point at the bandwidth edges. Appendix A shows that the bandwidth edges are well-
225   defined in fractional octave band representations of order N so that the quality factor can be evaluated
226   precisely as,

227
$$Q_N = \left[2^{\frac{1}{2N}} - 2^{-\frac{1}{2N}} \right]^{-1}. \tag{11}$$

228   From [1], and as shown in Appendices B and C, the characteristic time duration of the Gabor atom can
229   be represented as

230
$$T_n = M_N \, \tau_n \tag{12}$$

231   where M_N is a measure of the number of oscillations in the characteristic time duration of a wavelet. For
232   efficient computation all physical times are nondimensionalized and converted to equivalent sample
233   points by multiplying by the sample rate. If t is the time in seconds, the nondimensionalized time m is

234
$$m = f_s \, t \tag{13}$$

235   The approach is wavelet-agnostic up to this stage. Direct application of the ½ power points of the
236   spectrum of Gabor-Morlet wavelet at the band edges (Appendix C) yields
237

238
$$M_N = 2\sqrt{ln2} \; Q_N \approx 2\sqrt{2ln2} \; N \tag{14}$$

239   This last step can be tailored to other wavelet types to produce constant-Q variants. Adherence to the
240   specifications in Eqs. (10-14) lead to standardized and well constrained quantized Gabor atoms.
241

2.2. Binary Quantized Constant-Q Gabor Atoms

243   Gabor [2] extended the Heisenberg principle to define the time-frequency uncertainty principle, and
244   further proposed deconstructing signals into elementary waveforms referred to as time-frequency atoms
245   [2, 13]. These atoms provide the optimum compromise between time and frequency resolution and thus
246   maximize information density. The Morlet wavelet [14, 15], functional kin to the Gabor atom, was
247   developed for seismic applications and is much beloved by mathematicians. Much has been said and
248   written over the last 75 years about the merits, and limitations [e.g. 16], of the Gabor atom in diverse
249   fields of applied science ranging including quantum mechanics [e.g. 17], neurophysiology [e.g. 18] and
250   radar target recognition [e.g. 19].
251   Consider the translation and dilation of the familiar Gabor-Morlet mother wavelet

252
$$\Psi_N(m) = \frac{1}{\pi^{1/4}} exp\left(-\frac{m^2}{2}\right) \exp\left(iM_N m\right) \tag{15}$$

253   with dictionary [13]

254
$$\Psi_n[m - m'] = \frac{1}{\sqrt{s_n}} \Psi_N \left(\frac{m - m\prime}{s_n}\right) \tag{16}$$

255   which can be fully expressed as

256
$$\Psi_n(m - m') = \frac{1}{\pi^{1/4}} \frac{1}{\sqrt{s_n}} exp\left\{-\frac{1}{2}\left[\frac{m-m'}{s_n}\right]^2\right\} exp\left\{iM_N\left[\frac{m-m'}{s_n}\right]\right\} \quad (17)$$

257 where the mapping between the nondimensional scale s_n and the band period is

258
$$s_n = \frac{M_N}{2\pi} f_s \tau_n. \quad (18)$$

259 The constant-Q Gabor atoms are constrained to the discrete set of values

260
$$s_n = s_0 2^{\frac{n}{N}} = \frac{M_N}{2\pi} f_s \tau_0 2^{\frac{n}{N}}, \quad M_N = 2\sqrt{ln2} \, Q_N \quad (19)$$

261 with quality factor

262
$$Q_N = \left[2^{\frac{1}{2N}} - 2^{-\frac{1}{2N}}\right]^{-1} \approx \sqrt{2}N \quad (20)$$

263 defined by the ½ power points of the Fourier spectrum, quantized order N. For this functional form,
264 the wavelet admissibility condition can be represented as

265
$$M_N^2 \gg 1. \quad (21)$$

266 By quantizing constant-Q bands and the resulting wavelet scales it is possible to also discretize the
267 uncertainty in time and frequency of the resulting analyses. Since Gaussian pulses in general [12] and
268 Gabor atoms in particular are well-known to have the lowest time-frequency uncertainty [2, 13], they are
269 natural building blocks for uncertainty quantification. The Gaussian-wrapped oscillation in general, and
270 the Gabor atom in particular, meet the minimal value for the Heisenberg-Gabor uncertainty principle
271 (Appendix D), where the nondimensionalized temporal standard deviation σ_t and angular frequency
272 standard deviation σ_ω over all time and frequency satisfy

273
$$\sigma_{f_s t} = \frac{1}{\sqrt{2}} s_n \Rightarrow \sigma_{t_n} = \frac{1}{\sqrt{2}} \frac{M_N}{2\pi} \tau_n \quad (22a)$$

274
$$\sigma_{\omega/f_s} = \frac{1}{\sqrt{2}} s_n^{-1} \quad (22b)$$

275
$$\sigma_t \sigma_\omega = \frac{1}{2} \quad (22c)$$

276 which quantify time and frequency uncertainty discretely, minimally, and unambiguously.
277 Converting to physical time with $m = f_s t$ yields a more familiar Morlet representation

278
$$\Psi_n(t - t') = \frac{1}{(\pi s_n^2)^{1/4}} exp\left\{-\frac{1}{2}\left[\frac{f_s(t-t')}{s_n}\right]^2\right\} exp\left\{i\frac{2\pi f_n}{f_s}[f_s(t - t')]\right\} \quad (23)$$

279 where the scale s_n may be readily recognized as the standard deviation of a Gaussian envelope with
280 integration variable $m = f_s t$. This is very similar to the original form proposed by Gabor [2], and makes
281 intuitive sense as the oscillatory term is clearly exposed. However, the additional factor of f_s required to
282 nondimensionalize the numerator of the Gaussian envelope for numerical computation has indubitably
283 been an initial source of confusion amongst some physical scientists, author included.

284 **2.3. Quantum Order**

285 The recommended quanta for the Gabor atoms are positive integer band numbers n and the
286 preferred orders N as in [1]

287
$$n = 0, 1, 2 \ldots, \quad N = 1, 3, 6, 12, 24 \ldots \quad (24)$$

288 though the special orders $N=0.75$ and 1.5 are considered. The mother wavelet is uniquely defined (and
289 can be quantized) by the order N, although it is often specified by the more accessible variable M_N. The
290 mother wavelet is scale invariant. Each discrete atom in its dictionary is defined by its order N, its band
291 number n, and a refence scale at n=0. If the Gabor atoms remain within their quanta, there is only one

292 degree of freedom: the reference scale. The reference scale can be set by the data acquisition system (e.g.
293 the Nyquist frequency) or a standard frequency (e.g. 1kHz in audio applications). The scale schema can
294 also be set by a signal tuning frequency; the peak frequency for a 1 ton detonation is used in Section 3.
295 When integrating multi-sensor time series with different evenly and unevenly sampled data, it may be
296 preferrable to either use a standard reference frequency or time scale (e.g. 1 kHz) or a shared target
297 frequency. The resulting bands will be evenly spaced to standardize and facilitate multi-sensor cross-
298 correlations and data fusion. However, it is important to reinforce that the mapping from
299 nondimensional scale to physical time scale depends on the sample rate. Inversely, specifying a sample
300 rate f_s or a sample interval $\Delta\tau_s = 1/f_s$ permits conversion to physical time t and time scales τ_n from
301 the wavelet parameters,

302
$$t = \frac{m}{f_s}, \quad \tau_n = \frac{2\pi}{M_N}\frac{s_n}{f_s}, \tag{25}$$

303 and map to the physical frequencies

304
$$f_n = \frac{1}{\tau_n}, \quad \omega_n = 2\pi f_n . \tag{26}$$

305 It may be useful to think of the binary (base 2) order N as the quantized time and bandwidth stretch
306 factor of the Gabor atom; as the order increases, the wavelet stretches in time and narrows in bandwidth,
307 with each frequency band occupying a constant proportional frequency bandwidth that produces Q_N
308 oscillations at the band frequency in the time domain. As noted a few sentences up in sparser
309 mathematical notation, although in theory it is possible to use any integer band indexes n, the
310 recommended best practice is to use only nonnegative integers to represent temporal scales, with τ_0
311 corresponding to the smallest scale and ω_0 to the highest frequency below the Nyquist frequency.
312
313 This paper recommends atom quantization using the well-established fixed order N and quality
314 factor Q_N values of standard geometric binary intervals referred to as fractional octave bands in
315 acoustic and infrasound applications (Table 1).

316 **Table 1.** Quality factor Q and M_N for standard fractional octave bands of order N [1].

N	Q_N	M_N
1	1.4142	2.3548
3	4.3185	7.1907
6	8.6514	14.4055
12	17.3099	28.8229
24	34.6235	57.6519
48	69.2488	115.3067
96	138.4984	230.6150

317 [1] Dyadic base, G=2.

318 Appendix A develops a useful approximation for the quality factor Q_N of order N,

319
$$Q_N \approx \sqrt{2}N \approx 1.414\, N, \quad M_N = 2\sqrt{ln2}\, Q_N \approx 2\sqrt{2ln2}\, N \approx 2.355\, N \tag{27}$$

320 with exact equivalence for octave bands at N=1 (Table 2).

321 **Table 2.** Exact and approximate quality factor Q for standard fractional octave bands of order N [1].

N	Q_N	$Q_N \approx \sqrt{2}N$
1	1.4142	1.4142

3	4.3185	4.2426
6	8.6514	8.4853
12	17.3099	16.9706
24	34.6235	33.9411
48	69.2488	67.8823
96	138.4984	135.7645

 [1] Dyadic base, G=2.

These relations are seldom made explicit for constant-Q wavelet representations, which often leads to inadvertently creative interpretations and implementations. In traditional fractional octave bands, N is an integer with preferred numbers 1, 3, 6, 12, 24 and its half-power (-3 dB) band edges and center frequencies are well established so their Q can be readily computed (Tables 1 and 2). The band spectrum will overlap at the half-power point band edges to reduce (or at least regulate) spectral leakage and improve energy estimation. Dyadic wavelets use order N=1 and are weakly admissible ($M_N^2 \sim 5.54$); carefully handled they do lead to very sparse and fast computational implementations (e.g. [13]).

The estimate for Q_N in terms of the order N is useful for practical application where we wish to specify the number of oscillations Q_N in a window. If one abandons the bounds of the preferred bands, one can estimate the order for a wavelet that has any number of oscillations in its support window. Once N is estimated, exact values for the center frequencies and band edges can be computed from the expressions in Appendix A. These bespoke constant-Q bands will not meet binary (factor of two) center frequency recursions, but may be useful for highly customized tuning. Examples are provided in Table 3.

Table 3. Approximate quality factor Q and M_N for non-integer order N [1].

Q_N	$N \approx Q_N/\sqrt{2}$	M_N
1	0.7071	1.6651
2	1.4142	3.3302
4	2.8284	6.6604
8	5.6569	13.3209
16	11.3137	26.6417
32	22.6274	53.2835
64	45.2548	106.5670
128	90.5097	213.1340

 [1] Dyadic base, G=2.

Consider the curious case of a single oscillation in the window, where

$$N = \frac{3}{4} = 0.75, \quad Q_N = 1.04, \qquad M_N = 2\sqrt{ln2} \approx 1.74 \tag{28}$$

and Q is evaluated more precisely from the order N. Although intuitive and compact, the resulting wavelets are marginally admissible ($M_N^2 \sim 3$) and produce oddly spaced, but legitimate, constant-Q frequency bands that grow rapidly and hit only every fourth standard octave (power of two) every three bands. The window duration will be only 1.74 periods long and the spectral resolution of the Fourier

348 transform will be exceedingly sparse. Adding another oscillation per window (increasing the quality
349 factor to two), would correspond to

$$N = \frac{3}{2} = 1.5, \; Q_N = 2.14, \qquad M_N = 2\sqrt{ln2} \approx 3.57 \tag{29}$$

351 The resulting wavelets that are more admissible ($M_N^2 \sim 12.8$) but also produced oddly spaced constant-Q
352 frequency bands that land on every second standard octave every three bands. Third order bands hit
353 exact powers of two every third band and have around four oscillations per window (Appendix D).
354 Although it is possible to force center frequency scales, if best practices for band overlap are ignored one
355 will have a set of wavelet filter banks with substantial spectral leakage or gaps between adjacent bands,
356 and the possibility for excessively overdetermined or underdetermined results. This is what usually
357 happens with default parameters on most continuous or discrete wavelet transform algorithms. This
358 paper standardizes and regulates band spacing by asserting the relationship between order, bandwidth,
359 and duration. Since it is both silly and mathematically inadvisable (even inadmissible) to construct a
360 wavelet with less than one oscillation in its window, it is recommended that $Q \geq 1$. This suggests a
361 minimum order number (quantum) of *N*=3/4 for stable Gabor atoms, with *N*=1 yielding value exact
362 power of two (binary) bands.

363

364   It is possible to estimate the smallest possible universal binary scale from the Planck time, the
365 smallest measurable time scale

$$\Delta\tau_{Planck} = 10^{-43}s \sim 2^{-142}s. \tag{30}$$

367 Since the Planck time would be the smallest possible sample interval, the smallest oscillation that could
368 be observed would be at the universal Nyquist period

$$\tau_{min} = 2\Delta\tau_{Planck} \sim 2^{-141}s. \tag{31}$$

370 At the other end of the timeline, the age of the universe is estimated to be 13.8 billion years, or

$$\tau_{max} \sim 2^{58} \; s \tag{32}$$

372 so that the (presently) known universe can be encompassed in the range of ~200 temporal octave bands.
373 Computationally speaking, this is a small range of octaves that can be spanned by 200 temporal Gabor
374 atoms. Earth is estimated to be ~4.6 billion years old, covering around about 57 of those temporal binary
375 bands, and the oldest bones associated with Homo Sapiens-Sapiens are ~200,000 years old and within the
376 last 42 temporal sub-bands since Earth's inception. The human voice for average individuals ranges
377 between one and two octaves, and five octaves species-wide. A third order representation (*N*=3) of all
378 the times scales in the universe can be represented by only 600 temporal Gabor atoms. In principle it
379 would be possible to construct universal scales with $\tau_0 = 2^{-141}s$, whereas all timescales would occupy
380 temporal sub-bands, but it is not clear there would be practical value to it.

381

382   The beauty of the third order representation is that it is very close to the decimal representation,
383 with every ten 1/3 octaves producing a decade $(2^{10/3} \sim 10)$, and thus provide a geometrically elegant
384 compromise between ten-digit humans and binary digit machines. In addition to better meeting the
385 admissibility condition, third order bands will contain over 99% of the information within their octave
386 (Appendix E), making them compact temporal carriers. If the third order representation is used as the
387 base order (*N*=3), the preferred numbers are binary multiples (*N* = 3, 6, 12, 24 in Table 1), with a
388 proportional elongation in the wavelet support and increase in spectral resolution.

389

390   The nondimensionalized scale s_n at the Nyquist frequency is always the same regardless of
391 whether one uses the Plank scale or half the age of the known universe (which would be not only
392 impractical but not very informative as it would only leave one octave to process)

393
$$Q_1 = \sqrt{2}, \ M_1 = 2\sqrt{2ln2}, \ s_0 = \frac{M_1}{2\pi} \frac{\tau_{min}}{\Delta\tau_{Planck}} = \sqrt{\frac{ln2}{2\pi^2}} \tag{33a}$$

394
$$s_n = s_0 2^n \tag{33b}$$

395 Many software packages readily produce a Gabor-Morlet wavelet with default parameters. One of
396 the most common values is $M_N = 5$, which is close to order $N = 2$ (Table 4). Other common values of
397 the wavelet support correspond to $\Omega_N = 4$, $N = 1.7$ and the more reasonable $M_N = 8$ which is close to
398 preferred order $N = 3$.

399 **Table 4.** Approximate quality factor Q and order N for integer values of M.

M_N	$\sim Q_N$	N
1	0.600561204	0.4246609
2	1.201122409	0.8493218
4	2.402244818	1.698643601
5	3.002806022	2.123304501
6	3.603367226	2.547965401
8	4.804489635	3.397287201

400 [1] Dyadic base, G=2.

401 Because none of these specifications correspond to standard orders, the resulting wavelets will tend to
402 either overestimate (due to spectral leakage) or underestimate (due to spectral gaps between bands) the
403 energy within adjacent binary bands when forced, or will produce oddly spaced bands.
404
405 Although it is possible to quantize the constant-Q Gabor atoms using the order N, the quality factor
406 Q, or the multiplier M_N, the order is the most logical way to define the quanta of the wavelet. Describing
407 the proposed wavelet dictionaries of preferred orders as the quantized constant-Q Gabor atoms with
408 binary bases and overlapping ½ power points is rather awkward, and this paper proposes referring to
409 these constructs as quantized wavelets, quantum wavelets of order N, or Nth order Gabor atoms.
410 Although N=1 provides a sparse clean binary (with power of two steps in frequency) representation with
411 the tightest windows, the admissibility condition coupled with the better reconstruction capability
412 presented in the next section suggest that using N=3 as the base order is preferable, with the added
413 advantage that all subsequent preferred orders in Table 1 are binary factors of base order 3.

414 **2.4. Continuous Wavelet Transform Deconstruction and Reconstruction**

415 The continuous wavelet transform (CWT) of a function $g(x)$ is represented in [13] (Eq. 1.13) as

416
$$\mathcal{W}(g, u, s) = \langle g, \Psi_{u,n} \rangle = \int_{-\infty}^{\infty} g(x) \frac{1}{\sqrt{s}} \Psi^* \left(\frac{x-u}{s}\right) dx \tag{34}$$

417 where (*) represents the complex conjugate. The equivalent CWT for a discrete sequence of observations
418 (or a synthetic time series) $g(m)$ is the convolution of g with a scaled and translated version of $\Psi(m)$.
419 Consider the nondimensional Quantum mother wavelet of order N,

420
$$\Psi_N(m) = \frac{1}{\pi^{1/4}} exp\left(-\frac{m^2}{2}\right) \exp\left(iM_N m\right) \tag{35a}$$

421
$$\Psi_n[m] = \frac{1}{\sqrt{s_n}} \Psi_N\left(\frac{m}{s_n}\right) \tag{35b}$$

422 The discrete CWT can be expressed as

423
$$\mathcal{W}_n[m] = \sum_{m'=0}^{Mp-1} g(m') \Psi_n^*(m' - m) = g \circledast \Psi_n^*[m] \tag{36}$$

424   where the symbol $\circledast$ denotes a convolution [13], often computed using the discrete Fourier transform.
425   This is comparable to the expression in [20], although their convolution has no amplitude scaling as it is
426   corrected afterwards. The CWT coefficients $\mathcal{W}_{m,n}$ provide a measure of the degree of similarity between
427   the time series and the wavelet of scale index n while translating along the time index m. While exact
428   waveform reconstruction from the CWT is challenging (e.g. [21-22]), reference [20] provides an
429   approximate expression for the wavelet-filtered time series $g'(m)$. The reconstruction filter from the Nth
430   order Gabor atoms becomes,

431
$$g[m] \approx \frac{\pi^{\frac{1}{4}}}{N}\frac{1}{C_\delta}\sum_{n=0}^{Np-1}\frac{Re\{\mathcal{W}_n[m]\}}{\sqrt{s_n}} \tag{37}$$

432   Where $Re\{\ \}$ denotes the real part of the coefficients and the reconstruction factor C_δ is scale
433   independent and constant for wavelet function with fixed M_N. The reconstruction factor can be estimated
434   by comparing against known test functions. Reference [20] empirically computed a reconstruction
435   coefficient of $C_\delta = 0.776$ with $M_N = 6$, and [23] provides other estimates. Numerical evaluation shows
436   the product $NC_\delta \sim 2$, and the reconstruction approximation for the analytic (Appendix F) quantum
437   wavelet of arbitrary order is

438
$$g_{\mathbb{C}}[m] \approx \frac{\pi^{\frac{1}{4}}}{2}\sum_{n=0}^{Np-1}\frac{W_n[m]}{\sqrt{s_n}} \tag{38}$$

439   It is important to note how substantially different this expression is to the inverse discrete Fourier
440   transform, where

441
$$g_{DFT}[m] = \frac{1}{\sqrt{Np}}\sum_{n=0}^{Np-1}\hat{g}_{DFT}[n]\,exp(j2\pi mn/Np) \tag{39}$$

442   where $\hat{g}_{DFT}[n]$ are the Fourier coefficients. Unlike the discrete Fourier transform, the standard wavelet
443   reconstruction does not require multiplication by the mother wavelet. However, in the special case where
444   the atoms are well matched to the signal of interest, it of interest to consider the sparse set of coefficients
445   corresponding the complex time indexes $m_{n\,\mathbb{C}\,max}$ of the maximum energy, entropy, or SNR at each scale

446
$$g_{\mathbb{C}}[m] \approx \frac{\pi^{\frac{1}{4}}}{2}\sum_{n=0}^{Np-1}\frac{W_n[m_{n\,\mathbb{C}\,max}]}{\sqrt{s_n}}Re\{\Psi_n[m - m_{n\,\mathbb{C}\,max}]\} \tag{40}$$

447   where the maximum coefficient indexes can be computed separately for real and imaginary components.
448   This has the form of a sum over the dominant Gabor atoms for each scale. Since one is only considering
449   the maxima in a given record window, this is a very sparse representation consisting of the coefficient
450   and the time offset corresponding to the peak energy or entropy estimate. Numerical evaluation shows
451   that this last expression can be used to estimate the full analytic function representation as long as
452   reconstruction uses the complex coefficients but only the real atom function since the time shifts in the
453   Hilbert transform already include the $\pi/2$ time shift.

454   **2.5. Wavelet Information and Entropy**

455   One advantage of the constant Q wavelet representation is that it is possible to estimate the
456   information content and detectability of a signal in a band by applying the same set of wavelet transforms
457   to the signal and comparing them to the transform of a noise segment or model. Consider the definition
458   for Shannon's channel capacity [11], with

459
$$SNR_n = \frac{Ns_n + Sg_n}{Ns_n} = 1 + \frac{Sg_n}{Ns_n} \tag{41}$$

460
$$Ch_n = W\,log_2(SNR_n) \tag{42}$$

461 where Sg is the wavelet-transformed signal power and Ns is the wavelet-transformed noise power in a
462 band. Consider two possible estimates for the bandwidth W (since Shannon [11] left some room for
463 interpretation). The first estimate approximates W by the ½ power point bandwidth

$$\Delta f_n = \frac{f_n}{Q_N} \approx \frac{1}{\sqrt{2}} \frac{f_n}{N} \approx 0.7071 \frac{f_n}{N}. \tag{43}$$

465 The second estimates W using the Gabor box standard deviation for the angular frequency

$$\sigma_\omega = \frac{1}{\sqrt{2}} \frac{\omega_n}{M_N} \approx \frac{1}{4\sqrt{ln2}} \frac{\omega_n}{N} \approx \frac{\pi}{2\sqrt{ln2}} \frac{f_n}{N} \approx 1.8867 \frac{f_n}{N} \tag{44}$$

467 so that

$$\sigma_f = \frac{\sigma_\omega}{2\pi} = \frac{1}{4\sqrt{ln2}} \frac{f_n}{N} \approx 0.3003 \frac{f_n}{N}. \tag{45}$$

469 Taking the average of Δf_n and σ_f provides a compromise between the two possible estimates, and a
470 returns a tidy factor of ~0.5

$$Ch_n \approx \frac{1}{2} \frac{f_n}{N} log_2(SNR_n). \tag{45}$$

472 The effective SNR_G and therefore the "detectability" of a bandwidth-limited compressed pulse [12]
473 can be represented by the product of the Gabor time-bandwidth product (Appendix C) and the signal to
474 noise ratio

$$SNR_G = \sigma_t\,\sigma_\omega \times SNR_n. \tag{46}$$

476 Since the time-bandwidth product for the Gaussian wavelet is constant

$$\sigma_t\sigma_w = \frac{1}{2} \tag{47}$$

478 and the uncertainty of its Gabor box is at the minimum, the likelihood of the detection of a SOI in a given
479 band n is only proportional to its SNR.
480 Shannon's definition of the channel capacity was intended to represent the highest theoretical
481 transfer rate of information through an analog line. Since SNR is given in power, which is typically the
482 square of the signal amplitude, an unscaled binary log is off by a factor of two from the original data in
483 bits. To reconcile this definition with the original collection of a time series signal in floating point bits
484 (fbits), I define the binary SNR to match the signal rms amplitude as well as Shannon's units for the
485 information rate per band $Ch_{N,n}$ of the quantum compressed pulse as

$$bSNR_n = \frac{1}{2} log_2(SNR_n) = log_2(\sqrt{SNR_n}), \quad fbits \tag{48}$$

$$Ch_{N,n} = \frac{f_n}{N} \times bSNR_n, \quad shannons/s = fbits/s. \tag{49}$$

488 The increase in higher information delivery rate with increasing frequency is intuitive as more cycles are
489 transferred per second. As the order number increases, the bandwidth narrows and so the potential
490 information rate decreases. Less obvious is the decrease in high-frequency information with increasing
491 distance in a lossy transmission channel. Assuming the noise power remains unchanged, the decrease in
492 SNR with increasing scaled distance r from the source origin on a lossy acoustic channel can be
493 represented as

$$SNR = SNR_o \frac{exp(-\gamma f^2 r)}{r^{n_g}}. \tag{50}$$

495 where $n_g = 2$ for spherical geometric spreading in free space and $n_g = 1$ for cylindrical spreading in a
496 waveguide. The binary SNR can be represented as

$$SNR = \left[bSNR_0 - \frac{n_g}{2} log_2 r\right] - f^2 r\,(\gamma\,log_2 e). \tag{51}$$

498   The term in parenthesis shows the expected reduction of one bit per doubling of distance for spherical
499   spreading $(n_g = 2)$. The last term suggests the frequency dependence of the channel capacity in a lossy
500   acoustic medium may have the general form

501
$$Ch_n \sim \alpha(log_2 r)\, f - \beta(r)\, f^3 \tag{52}$$

502   so that with increasing range the optimal information transmission frequency shifts to lower frequencies.
503   One may readily extend the binary SNR definition to the measure of relative power

504
$$bR = log_2\left(\sqrt{\frac{S}{S_{max}}}\right) = \frac{1}{2} log_2\left(\frac{S}{S_{max}}\right), \quad fbits \tag{53}$$

505   and the -3dB half-power point becomes the -1/2 bit power point.
506   The entropy of a signal of interest can be estimated by the wavelet coefficients. A practical approach
507   is described in [24]. The information content of each scale n at the time step m can be estimated from the
508   wavelet energy. First estimate the complex wavelet coefficient energy from

509
$$E_{m,n} = \left|Re\{\mathcal{W}_{m,n}\}\right|^2 + j\left|Im\{\mathcal{W}_{m,n}\}\right|^2. \tag{54}$$

510   The total energy in a given record can be estimated from

511
$$E = \sum_m \sum_n \sqrt{E_{m,n} E_{m,n}^*} \ . \tag{55}$$

512   The complex probability of $\mathcal{W}_{m,n}$ in the record is

513
$$p_{m,n} = \frac{E_{m,n}}{E} \tag{56}$$

514   where

515
$$\sum_m \sum_n p_{m,n}\, p_{m,n}^* = 1 \ . \tag{57}$$

516   The log energy entropy (lee) per coefficient can be defined by the binary logarithm
517

518
$$e_{lee} = log_2\left(p_{m,n}^2\right) = 2log_2\left(p_{m,n}\right) \tag{58}$$

519
520   where it should be noted that the factor of two scaling coefficient does not alter the relative weight of
521   each coefficient. The Shannon entropy (se) per CWT coefficient is defined as
522

523
$$e_{se} = -p_{m,n} log_2\left(p_{m,n}\right) \tag{59}$$

524
525   with corresponding complex versions that separate the real and imaginary components. These entropies
526   can be readily evaluated to construct noise models from the lowest entropy components. If a stable noise
527   model can be constructed from the record or from prior knowledge of the environment and transmission
528   channel, SNR estimates can be computed and the process repeated to evaluate the dimensionless binary
529   log of the SNR

530
$$bSNR_{m,n} = \frac{1}{2} log_2\left(SNR_{m,n}\right) \tag{60}$$

531
532   and the product of the ratio and the binary ratio (RbR), an entropy-like nondimensional metric of the
533   SNR that can be readily evaluated to identify and extract the wavelet coefficients would be most
534   representative of a signal of interest,
535

536
$$RbR_{m,n} = SNR_{m,n} \times bSNR_{m,n}. \tag{61}$$

3. Discussion: Explosion Case Study

The methods presented in this paper are foundational: the intention is to use the Gabor atoms as fundamental building blocks with minimal time-frequency uncertainty and high information density. These methods are illustrated and discussed in the context of a blast pulse. Consider a normalized transient wave function characteristic of an explosion. Suppose one wanted to construct sparse wavelet representation of a pulse with peak energy at 6.3 Hz, corresponding to the detonation of one metric ton on TNT observed at 1 km. It is known [e.g. 7] that at some distance from the source this center frequency may drop by an octave (factor of two in frequency) or more, as well as become stretched out (dispersed) in time due to propagation effects. A theoretical source pressure function for the detonation of high explosives was developed in some detail in [7] with one kiloton as the case study, and is used here to construct a representative synthetic waveform for a one (metric) ton detonation. Define τ_c

$$\tau_c = 4\tau_p, \quad f_c = \frac{1}{\tau_c}, \quad \omega_c = 2\pi f_c \tag{62}$$

as the pseudo-period of a blast pulse corresponding to the peak spectral energy at the frequency f_c and angular frequency ω_c, where τ_p is the time duration of the initial positive pulse traditionally used in blast physics. The nondimensionalized time scale is

$$\hat{t} = \frac{t}{\tau_p} = 4\frac{t}{\tau_c} \tag{63}$$

The form of the amplitude-normalized source pressure function for an explosive blast [7] can be represented as

$$g(\hat{t}) = (1 - \hat{t}), \quad 0 \le \hat{t} \le 1 \tag{64a}$$

$$g(\hat{t}) = \frac{1}{6}(1 - \hat{t})\left(1 + \sqrt{6} - \hat{t}\right)^2, \quad 1 < \hat{t} \le 1 + \sqrt{6}. \tag{64b}$$

This pulse has an associated analytic function $g_{\mathbb{C}}(\hat{t})$ discussed in Appendix F. Since the theoretical Hilbert transform has some unresolved issues, the numerical Hilbert transform [25] is used for comparison.

Note that the amplitude is not used in this exercise because in some cyber-physical systems, such as smartphones, the amplitude response of on-board sensors may not be known. However, sensor dynamic range is usually specified and available (e.g. int16, float32) and can be used for signal scaling relative to the full range or the noise.

The normalized pulse has zero mean (conservation of momentum) and its theoretical variance is

$$\sigma_p^2 = \int_{-\infty}^{\infty} g^2(\hat{t})\, dt = 0.95\frac{\tau_c}{8}. \tag{65}$$

The complex Fourier transform $\hat{g}(j\hat{\omega})$ of this pulse is

$$\hat{g}(j\hat{\omega}) = \frac{\pi}{2\omega_n}\left[\frac{1 - j\hat{\omega} - e^{-j\hat{\omega}}}{\hat{\omega}^2} + \frac{e^{-j\hat{\omega}(1+\sqrt{6})}}{3\hat{\omega}^4}\left\{j\hat{\omega}\sqrt{6} + 3 + e^{j\hat{\omega}\sqrt{6}}\left[3\hat{\omega}^2 + j\hat{\omega}2\sqrt{6} - 3\right]\right\}\right] \tag{66}$$

where $\hat{\omega} = \frac{\pi}{2}\frac{\omega}{\omega_c} = \frac{\tau_c}{4}\omega = \tau_p\omega$ and the peak in the spectrum is at $\omega = \omega_c$. Note there are at least two pseudoperiods of importance evident in the main blast pulse: the main spectral pseudoperiod τ_c and positive phase pseudoperiod of $2\tau_p$. Near the source the positive phase pseudoperiod will dominate as it has the highest energy and bandwidth. With increasing distance and high-frequency attenuation the main pseudoperiod becomes more prominent and may also be downshifted in frequency [7]. However, additional scales can be introduced by reflection and refraction in the transmission channel that can induce phase shifts often modeled with Hilbert transforms (Appendix F).

578
579   The power spectra of real digital signals are usually expressed using only the positive frequencies
580   up to the Nyquist frequency, where the unilateral spectral density $Pg(\hat{\omega})$ is defined as
581

$$Pg(\hat{\omega}) = 2|\hat{g}(j\hat{\omega})|^2 = 2\,\hat{g}(j\hat{\omega})\hat{g}^*(j\hat{\omega}). \tag{67}$$

583   Since the target signature corresponds to a one metric ton (1000 kg) blast, the analysis concentrates
584   on a target frequency of 6.3 Hz [7]. The general procedure for constructing target-tuned fractional binary
585   bands of order N is to define a set of base-2 scales around the center or reference frequency
586

$$f_c = 6.3\text{Hz}, \ \ f_j = f_c 2^{\frac{j}{N}}. \tag{68}$$

588   The upper limit is set by the Nyquist frequency, which means that the center frequency and its band
589   edges should be below the Nyquist and the ½ power point of the anti-aliasing filter. A conservative
590   estimate is

$$f_{j\,max} = f_{tg}2^{\frac{j\,max}{N}} < \frac{f_s}{2} \ \Rightarrow \ j\,max < floor\left(Nlog_2\left[\frac{f_s}{2f_{tg}}\right]\right). \tag{69a}$$

592   The lower limit is set by the largest data window duration T

$$f_{j\,min} = f_{tg}2^{\frac{j\,min}{N}} > \frac{2}{T} \ \Rightarrow \ j\,min > ceil\left(Nlog_2\left[\frac{2}{Tf_{tg}}\right]\right) \tag{69b}$$

594   so the center frequencies are defined by

$$f_j = f_c 2^{\frac{j}{N}}, \ j \in [j\,min, j\,max] \tag{70}$$

596   which will be sufficient information to compute the Morlet scale s_n. If one must convert to a sorted,
597   monotonically increasing pseudoperiod, let

$$\tau_j = \frac{1}{f_j}, \ \ \tau_0 = min(\tau_j) \tag{71}$$

599   and restart the counter for the period

$$\tau_n = \tau_0 2^{\frac{n}{N}}, \ \ n \in [0, j\,max - j\,min = length\,(f_j)]. \tag{72}$$

601   This re-indexing is much easier to do numerically than to describe algorithmically. For the purposes of
602   illustration and demonstration, let's choose a signal frequency that exactly matches the target frequency;
603   if this example fails there is no purpose in continuing. A sample rate of 200 Hz will be more than sufficient
604   for this example. Gaussian noise with a standard deviation that is one bit below the signal variance (factor
605   of 1/2) is added, and then anti-alias filter all frequencies below Nyquist. The analytic function is
606   computed numerically from the real pulse for later comparisons with the wavelet-reconstructed signal.
607   The CWT scalogram is computed using the complex nondimensional mother quantum wavelet of
608   order N. The complex Gabor-Morlet wavelet in SciPy [26] is represented by the function
609   scipy.signal.morlet2, and has the desired canonical form,

$$\Psi_H(m) = \frac{1}{\pi^{1/4}}exp\left(-\frac{m^2}{2}\right)\exp\left(iM_N m\right) \tag{73a}$$

$$\Psi_{u,n}(m) = \frac{1}{\sqrt{s_n}}\Psi_H\left(\frac{m-u}{s_n}\right) \tag{73b}$$

$$s_n = s_0\,2^{\frac{n}{N}} = \left[\frac{M_N}{2\pi}f_s\tau_0\right]2^{\frac{n}{N}} = \frac{M_N}{2\pi}\frac{f_s}{f_n} \tag{73c}$$

$$T_n = [M_N\tau_0\,]2^{\frac{n}{N}} = \frac{M_N}{f_n} \tag{73d}$$

614
$$M_N = 2\sqrt{ln2}\, Q_N \tag{73e}$$

615
$$Q_N = \left[2^{\frac{1}{2N}} - 2^{-\frac{1}{2N}} \right]^{-1} \tag{73f}$$

616
617 The only free variables are the order N, the smallest time scale τ_0, and the sample rate f_s. Although that
618 the nondimensionalized scale will change with the sample rate, but the final results can always be
619 returned to the physical domain frequencies f_n. The nominal number of points per window can be
620 estimated from $f_s T_n$. The complex wavelet coefficients can be readily computed from the real part of the
621 discrete version of the blast source-time function $p(m)$
622

623
$$W_n[m] = \sum_{m'=0}^{Mp-1} p(m')\Psi_n^*(m'-m) = p \circledast \Psi_n^*[m]. \tag{74}$$

624 After minor conditioning, the SciPy CWT function [26] promptly invokes the convolution function. This
625 is computationally expensive: we've turned a time series with Mp points into a complex 2[Mp x Nbands]
626 array of band-passed waveforms. The terms wavelets and wavelet filter banks are often used
627 interchangeably in the context of the CWT.
628   The wavelet-filtered reconstructed complex analytical signal can be approximated from

629
$$g_{\mathbb{C}\,ij}[m_k:m_l] \approx \frac{\pi^{\frac{1}{4}}}{2} \sum_{n=i}^{j} \frac{W_n[m_k:m_l]}{\sqrt{s_n}} \tag{75}$$

630 where the i, j indexes indicate that one may choose selected scales for the reconstruction over selected
631 time indexes $m_k:m_l$ corresponding to the wavelet coefficients that best represent a signal of interest
632 during the time interval of relevance. The scaled wavelet coefficients for the binary band decomposition
633 are shown in Figure 1. Figure 2 shows a comparison of the input synthetic analytic record and the analytic
634 signal reconstruction (summed over all scales) for the octave band representation. In Figure 1 the CWT
635 wavelet amplitudes are scaled by the reconstruction coefficients.
636
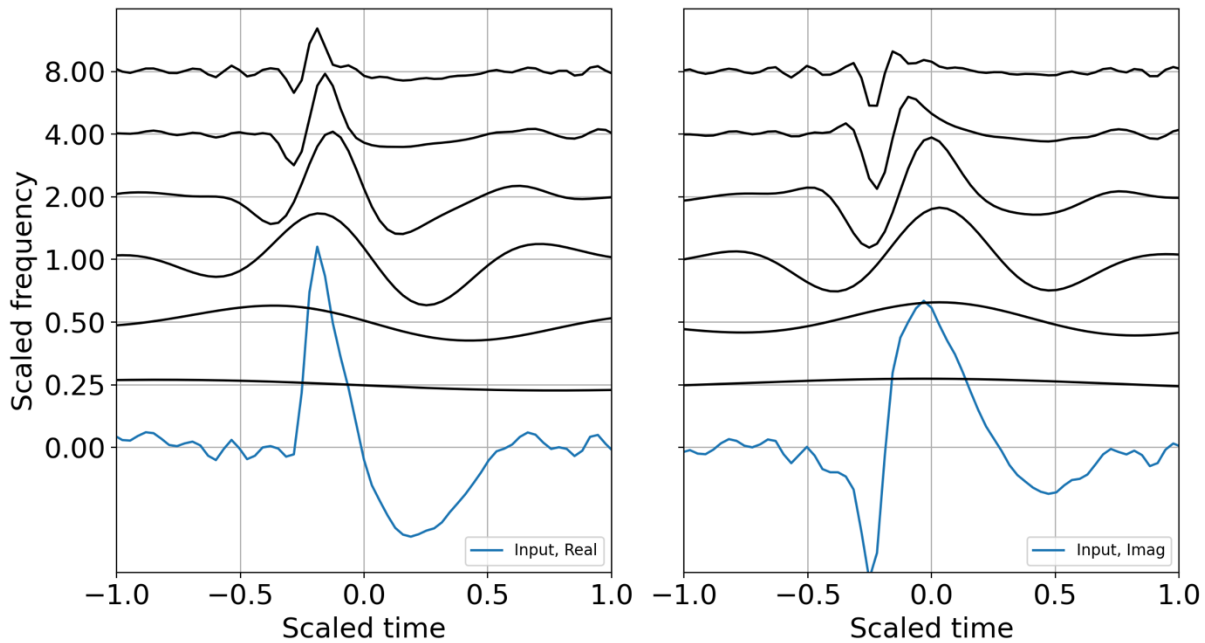
637
638 Figure 1. Analytic signal from mathematical equation, computation with SciPy Hilbert, and the CWT
639 reconstruction. (**a**) Real part; (**b**) imaginary part. The wavelets were evaluated in binary bands (N=1) and

640　　　constructed around the target frequency of 6.3 Hz, which scales frequency and time. The real input
641　　　waveform and its computed Hilbert transform are displayed in blue at the zero frequency.

642

643
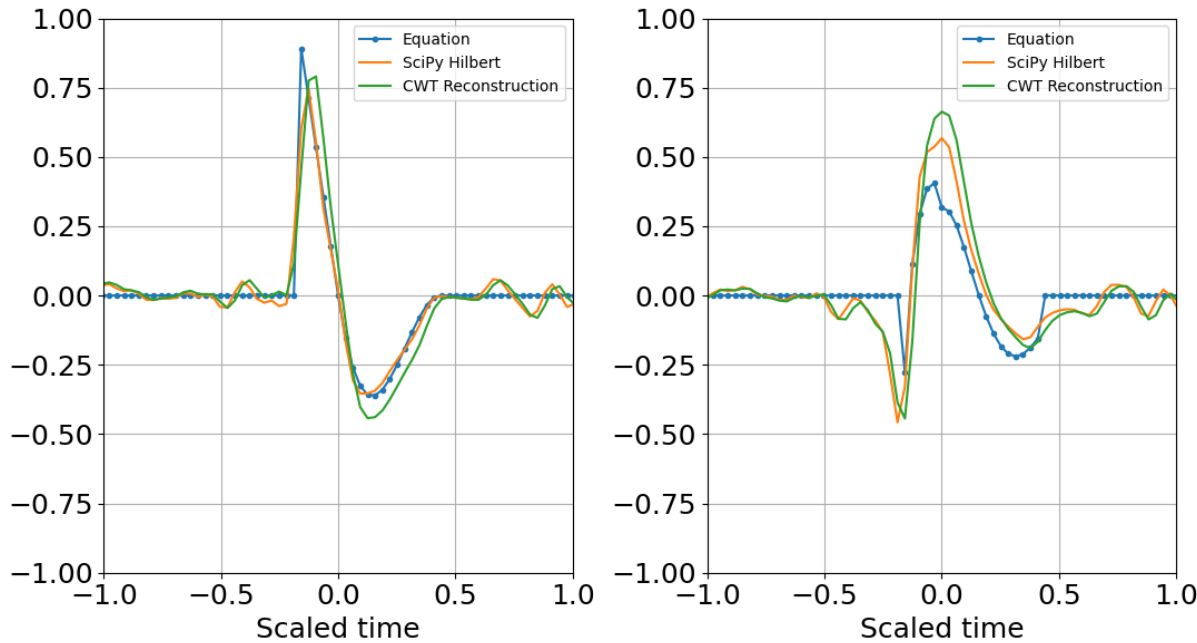
644　　　Figure 2. Wavelet reconstruction with binary bands. (a) Real part; (b) Imaginary part. The Equation
645　　　waveform has no noise and is not filtered, whereas Hilbert has Gaussian noise and has been anti-aliased
646　　　filtered.

647　　The reconstruction process recovers the original dimensionality of the time series but returns its Hilbert
648　　transform, so the total dimensionality may be doubled (2Mp sample points). If only the original real
649　　signal is desired, then the dimensionality is unchanged.
650
651　　The next steps estimate entropy and SNR, and consider sparse signal representation. Although binary
652　　bands are adequate for characterizing this signal, and are routinely used in the discrete wavelet
653　　transform, I take advantage of the flexibility offered by the CWT and use third order bands (N=3) for the
654　　examples that follow. One of the benefits of order 3 bands is that the admissibility condition is better met
655　　and scales are recursive in powers of 2 and 10 (e.g. [1]). As presented in Appendix D, third order bands
656　　will contain over 99% of the Gabor box variance within an octave and within 80% of the full window T_n,
657　　reducing spectral leakage. If, in addition, one wants a factor of two accuracy in explosive yield estimates,
658　　1/3 octave resolution is a minimum requirement. A third order band wavelet decomposition is presented
659　　in Figure 3, and is the equivalent of the scalograms usually represented as color plots. The wire mesh
660　　representation illustrates the simplicity of the CWT decomposition. The difference between Figure 3 and
661　　Figure 5 is that the first scales the raw CWT coefficients by the reconstruction scaling, whereas Figure 5
662　　shows the raw coefficients.
663

664
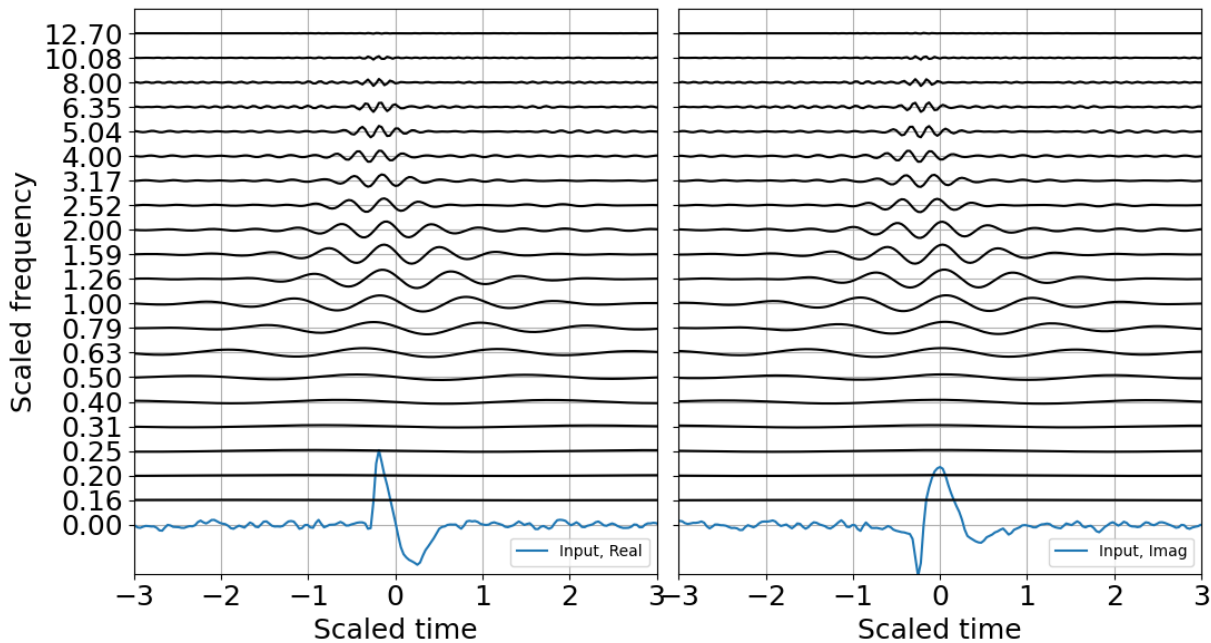
Figure 3. Wavelet decomposition with 1/3 octave bands, with CWT amplitudes scaled by the
reconstruction coefficients. (a) Real part; (b) Imaginary part. As with Figure 1, the input waveform is
displayed at the zero frequency.

668
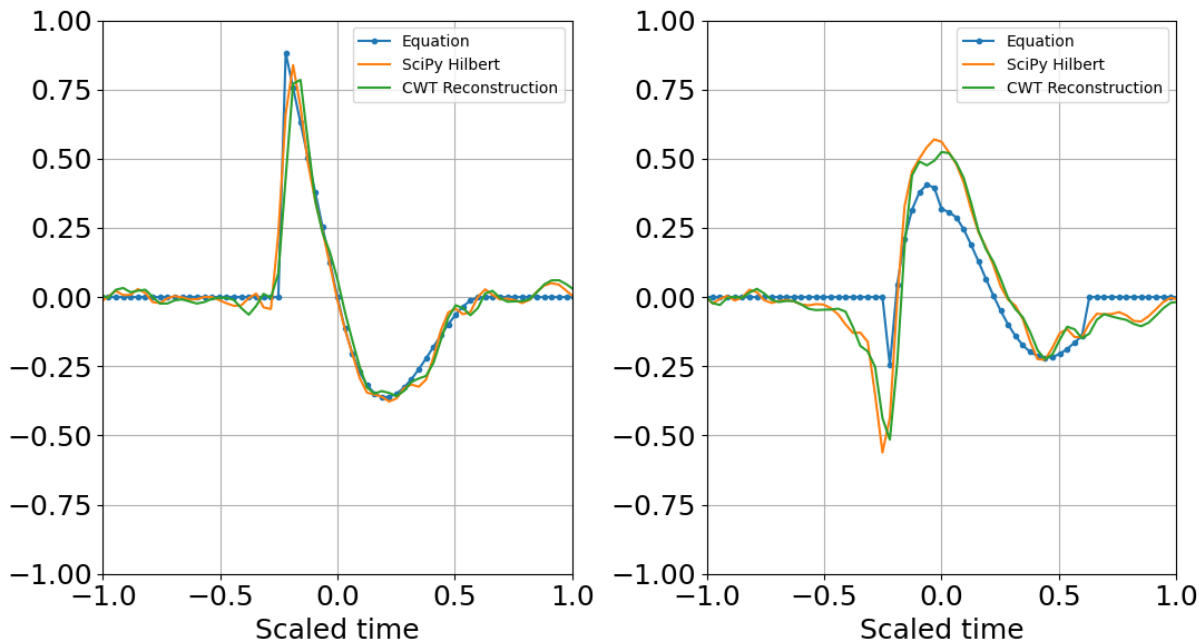
Figure 4. Wavelet reconstruction with 1/3 octave bands. (a) Real part; (b) Imaginary part.

670

671
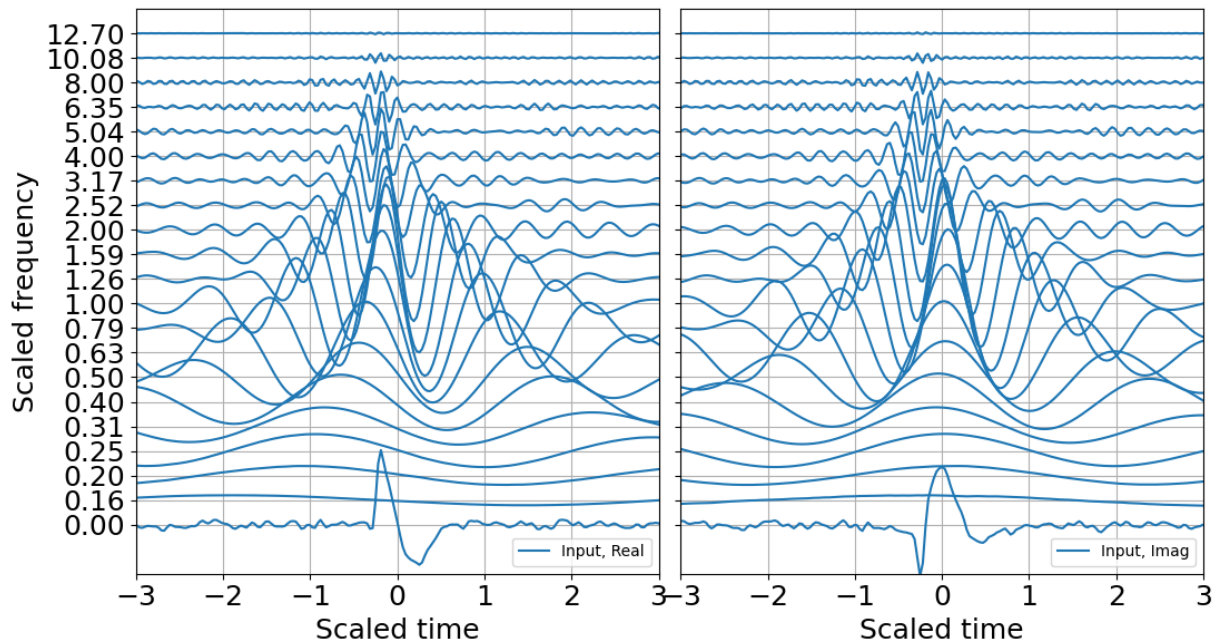
Figure 5. Wavelet decomposition in order 3 binary bands, raw CWT amplitudes. (a) Real part; (b) Imaginary part.

The energy probability distribution is constructed from the wavelet coefficients to estimate entropy, as discussed in the previous section. The log energy entropy looks like any other scalogram and does not add much value, but the Shannon entropy plot is interesting and well scaled (Figure 6). The peak entropy is at the blast center frequency, as expected.

680
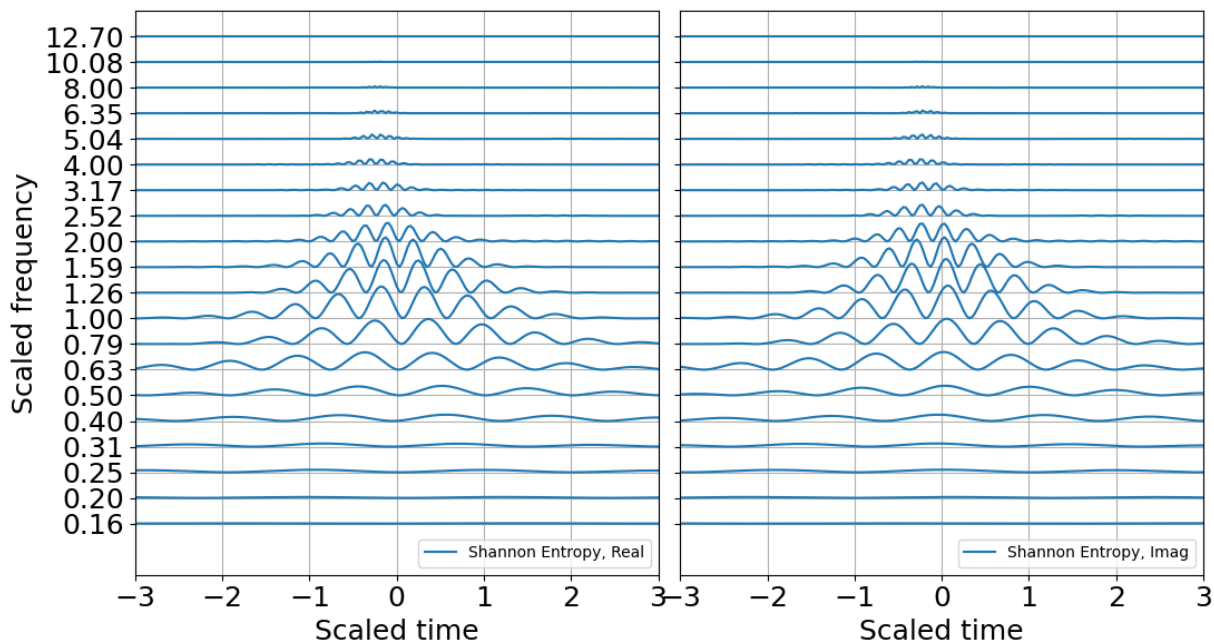
Figure 6. Shannon entropy in order 3 bands from raw CWT amplitudes. (a) Real part; (b) Imaginary part.

682
683   Next a noise model is constructed to build the SNR and to establish criteria for standardized and
684 reproducible sparse signal representation. Many are the ways to characterize noise, and few of them
685 accurately characterize non-stationary noise over brief observation windows. An incorrect noise model
686 can penalize the signal passband and degrade the signal SNR. For the white noise model with variance
687 that is one bit below the signal variance, the CWT of the noise (Figure 7) shows how the high-frequency
688 oscillations are adequately sampled whereas the low-frequency oscillations are undersampled. This leads
689 to instability if the noise is only estimated over a brief observation record. In principle, once can build a
690 noise model over a substantial period of time to obtain better statistical significance under the assumption
691 the noise is stationary. This can be a tenuous assumption in some circumstances. Noise studies are
692 beyond the scope of this paper; the noise spectrum is flattened by using the mean of the noise coefficients
693 to estimate the band-averaged noise level.
694
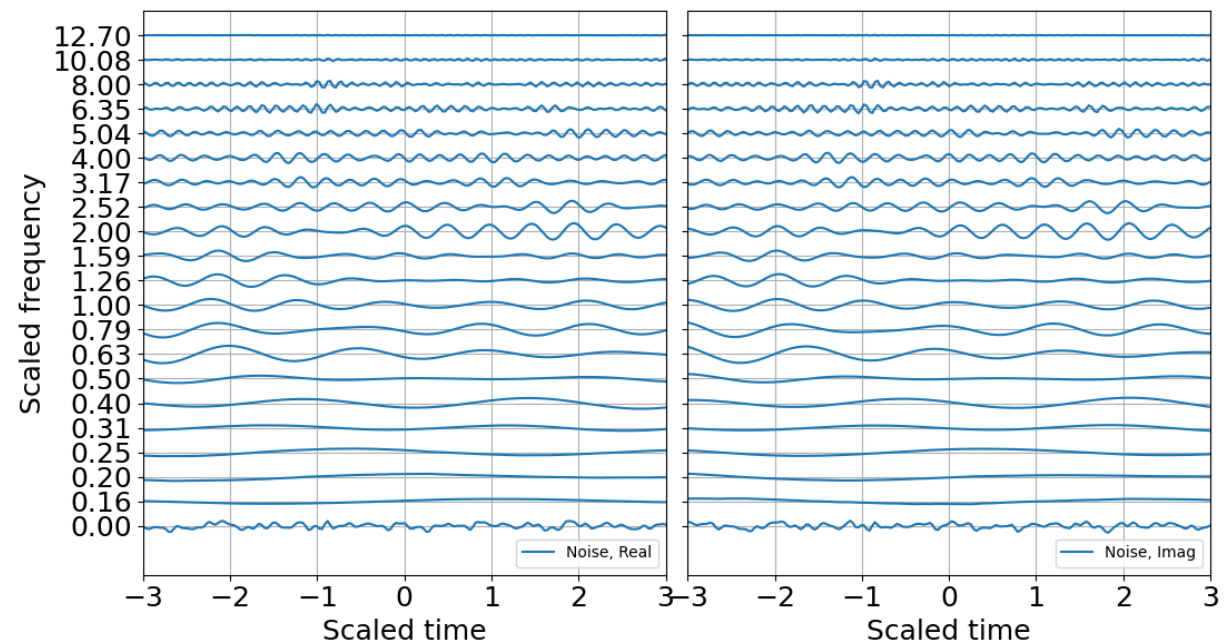
695
696   Figure 7. Raw CWT of noise in 1/3 octave bands. (a) Real part; (b) Imaginary part.

697   As expected, the binary SNR appears much like the log energy entropy since they are both scaled
698 by a constant value, with the former over the band-averaged noise and the latter over the total energy.
699 The SNR RbR, as described in the previous section, should also look very much like the entropy, except
700 it would be zero for SNR of unity and positive for SNR>1. The SNR RbR is shown in Figure 8, and
701 unsurprisingly, matches the Shannon entropy plot. These are good news; the entropy plot requires
702 constructing an energy distribution that scales with the record, whereas the SNR requires constructing a
703 noise model that is mostly independent of the record and should have more stability as long as the
704 ambient noise is approximately stationary or can at least be adequately modeled. If one is curating data
705 for machine learning training, the entropy would be a good metric for picking and annotating, as well as
706 for refining noise models. If one is trying to trigger or detect signals operationally, the SNR may be a
707 preferable metric as it makes no assumptions about the total energy in a record and only scales relative
708 to a (preferably) stable noise representation.

709
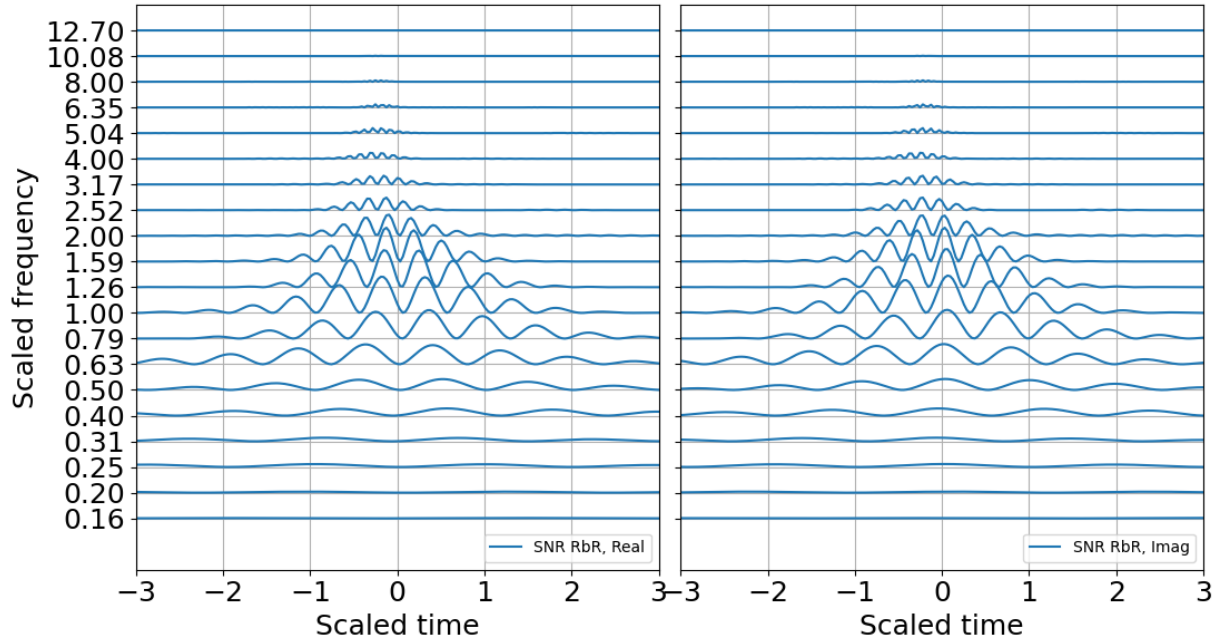
710   Figure 8. SNR RbR in 1/3 octave bands. (a) Real part; (b) Imaginary part.

711   One may use the CWT coefficient energy, the Shannon entropy, or the SNR RbR to test the feasibility of
712   the sparse Gabor atom superposition. Suppose we use any of these Np scales x Mpoint time matrices to
713   identify the peak contributions over the record, and identify the complex time indexes as $m_{\mathbb{C}\,max}$. The
714   quantum wavelet superposition would be expressed as
715

716
$$g_{\mathbb{C}\,ij}[m_k:m_l] \approx \frac{\pi^{\frac{1}{4}}}{2} \sum_{n=i}^{j} \frac{w_n[m_{n\,\mathbb{C}\,max}]}{\sqrt{s_n}} Re\{\Psi_n[m_k:m_l - m_{n\,\mathbb{C}\,max}]\} \qquad (76)$$

717
718   where the dimensionality of the representation is reduced to the complex coefficients and time indexes.
719   Since the wavelet function can be reproduced for any time index, the time array need not be stored. In
720   other words, if there are 20 scales, there will be 20 real coefficients and time offsets and 20 imaginary
721   coefficients and time offsets, with total dimensionality of 4x20 = 80 parameters. If there is sufficient SNR
722   and the signal is band limited it is possible to further reduce dimensionality by removing any coefficients
723   below a specified threshold that may be fitting to noise (e.g. overfitting). Figure 9 shows the result of
724   reconstruction from the superposition of all the top atoms of the 20 scales, and Figure 10 shows
725   reconstruction from a sparser set of 12 scales with the highest SNR RbR. Similar results were obtained
726   using the Shannon entropy. The Gaussian noise standard deviation for these two runs was one bit below
727   the signal standard deviation.

728
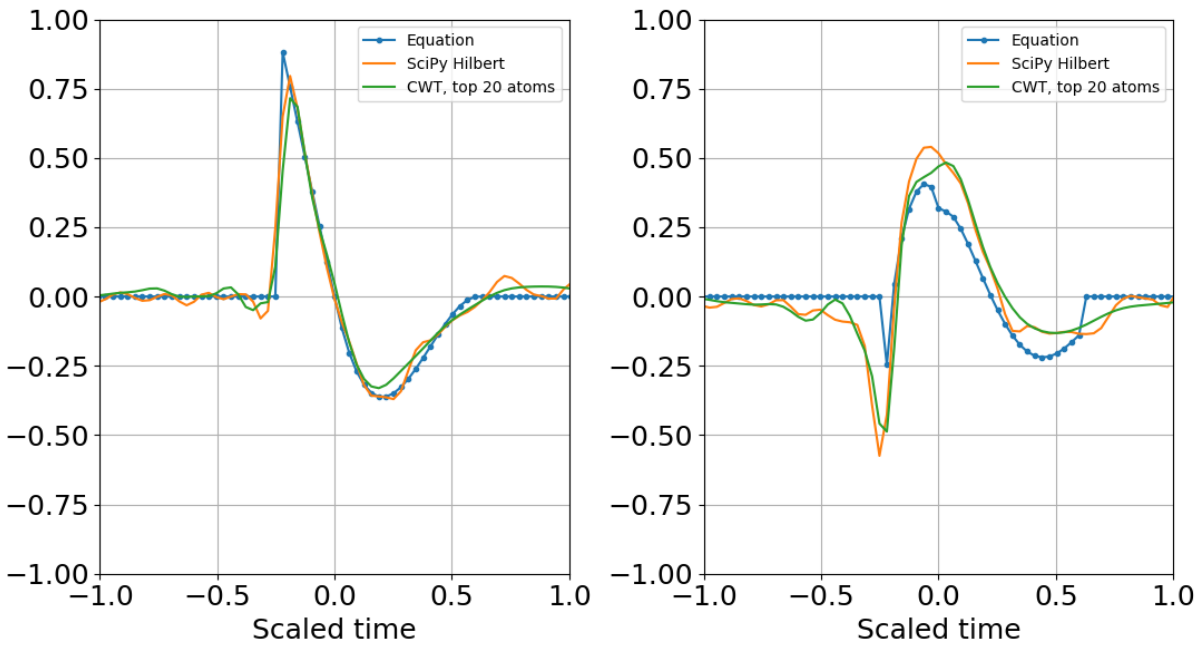
729 Figure 9. Superposition of largest SNR entropy coefficients per band using all twenty 1/3 octave bands.
730 (a) Real part; (b) Imaginary part. The noise standard deviation is one bit below the signal's. Dimensionality
731 is reduced to the number of coefficients and their corresponding time shifts.

732
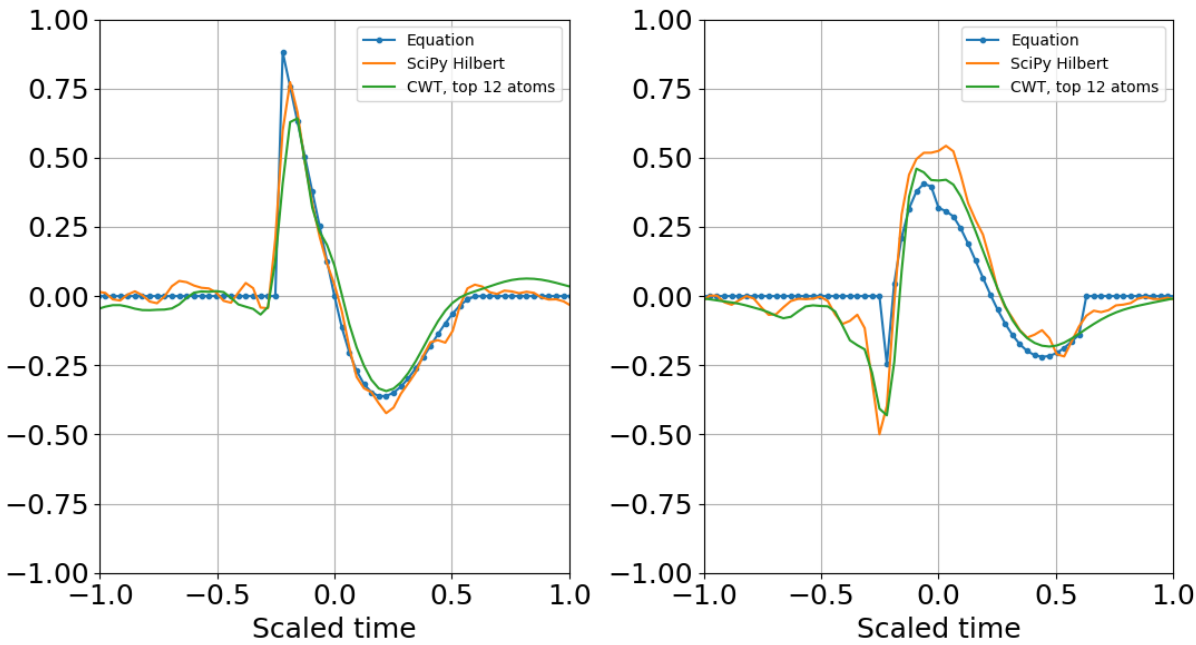
733 Figure 10. Superposition of largest coefficients per band within 4 bits of the peak SNR entropy. (a) Real
734 part; (b) Imaginary part. Dimensionality is further reduced by applying the cutoff.

735 Increasing the noise standard deviation by a factor of two (one bit) still permits reconstruction from
736 superposition (Figure 11), and increasing by another bit also allowed atomic reconstruction (Figure 12).

737
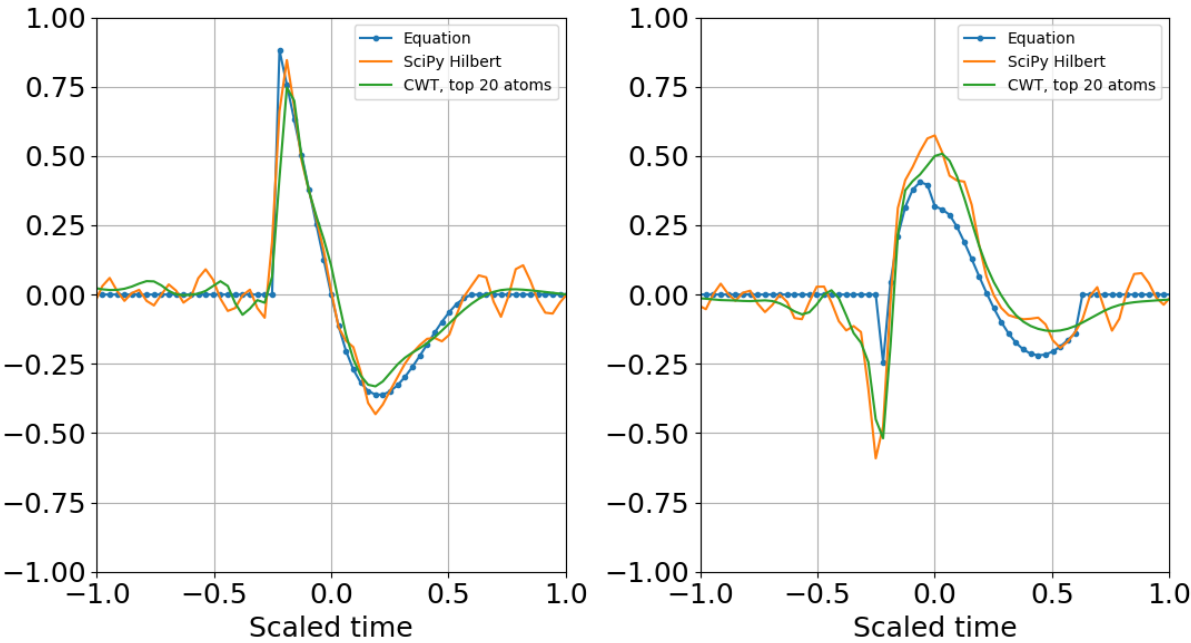
738 Figure 11. (a) Real part and (b) imaginary part of the original and reconstructed waveform. Increasing the
739 noise amplitude so that its variance is the same as the signal variance still permitted reconstruction from
740 the superposition of the largest atoms per band.

741
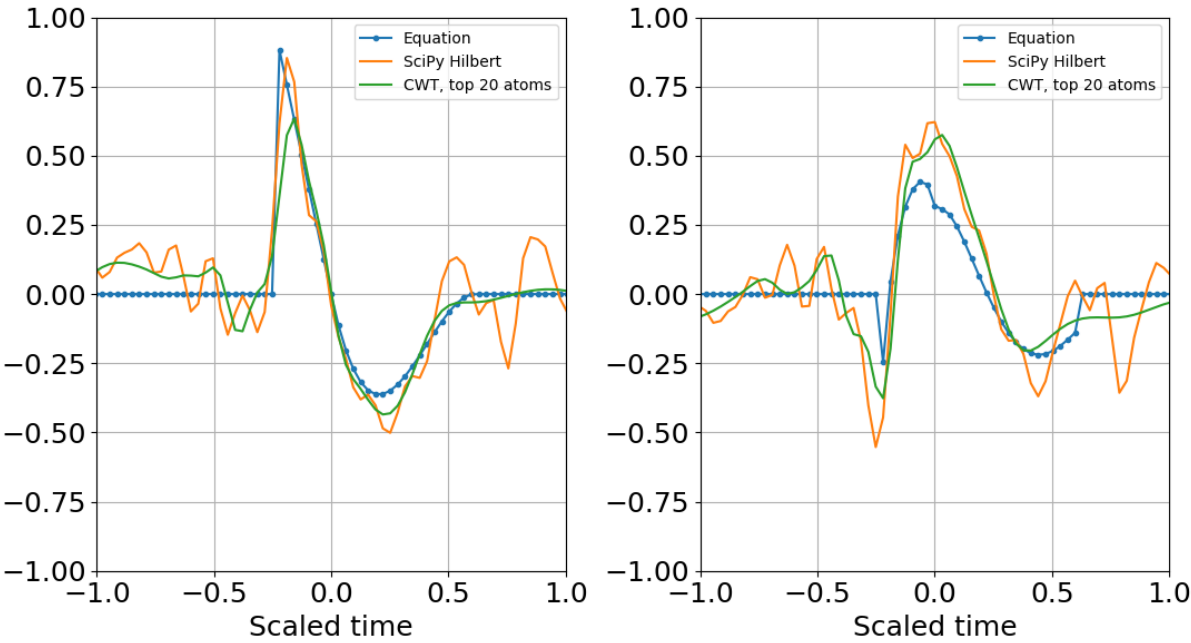
742 Figure 12. (a) Real part and (b) imaginary part of the original and reconstructed waveform. Increasing the
743 noise standard deviation is one bit above the signal standard deviation also allowed reconstruction from
744 the quantum wavelet superposition.

745 There is no end to the number of sensitivity studies that can be performed; in addition to other SNR tests
746 Shifting the peak blast frequency away from the nominal target frequency still returned a stable

747 reconstruction. Increasing the order past N>6 only worsened the fit to the target waveform, increasing
748 dimensionality and computational cost while decreasing reconstruction fidelity. This is expected from
749 using a wavelet that does not match the target signature.

750 **5. Concluding Remarks**

751   This paper proposes a transition to binary metrics for digital data and introduces a standardized,
752 quantized variation of the Gabor atoms with binary bases, optimal time-frequency resolution, and clear
753 spectral energy containment. A binary entropy-like metric for the SNR is proposed and used to extract
754 the peak coefficients to evaluate the performance of the superposition of Gabor atoms against the more
755 traditional CWT reconstruction. Although the immediate application is the analysis of time series data
756 collected with cyber-physical systems such as smartphones, the methods presented in this paper should
757 be transportable to other types of digital records and can be extended to other wavelet families.
758   I used a synthetic for a one metric ton detonation in Gaussian noise as an example, and did not
759 include the blast amplitude as a key parameter so as to concentrate on the entropy and SNR, which are
760 both dimensionless scaled quantities. Observations collected close to an explosion should have brief
761 durations and a high SNR; for short pulses it is advisable to use Gabor atoms of small order (N=1-6). Due
762 to cube root yield scaling, the third order bands will provide a yield resolution – and uncertainty - of a
763 factor of two, and one-sixth order bands will return square root of two yield resolution. In other words,
764 the uncertainty of yield estimates obtained with the quantum wavelet would be inversely proportional
765 to the cube root of the band order. Acceptable signal reconstructions were obtained from the CWT
766 coefficients as well as the superposition of the peak third order Gabor atoms for the blast signature. At
767 increasing distance from the source, the peak frequency is expected to drop [7] and the pulse disperses
768 over time. This opens up the possibility for stable 6 and 12 order analyses with a corresponding
769 improvement in yield resolution. Future work will concentrate on such dispersed signatures as well as
770 consider other types of CW signatures that would be well matched to higher-order Gabor atoms.
771   The methods developed have the goal of providing a tunable, standardized framework for signature
772 feature extraction to be used for signal classification, and should be well suited for dictionary learning
773 [13].

774
775
776

777 **Appendix A. Generalized Constant Q Bands**

778   This work builds on the Infrasonic Energy, Nth Octave (Inferno) framework [1], which has been
779 implemented in infrasound array processing algorithms for nuclear monitoring applications (e.g. [3-4])
780 Logarithmic constant-bandwidth, also referred to as proportional frequency or constant quality factor
781 (Q) bands, are traditionally defined by their scaled bandwidth

782

783
$$\frac{\Delta f}{f_n} = \frac{f_H - f_L}{f_n} = \frac{1}{Q},$$

784

785 where f_n is the center frequency of band number n and f_H and f_L are referred to as the upper and lower
786 band edge frequency, respectively. Defining the center, upper, and lower band edge *periods* as

787

788
$$\tau_n = \frac{1}{f_n}, \ \tau_H = \frac{1}{f_L}, \ \tau_L = \frac{1}{f_H},$$

789 then

790
$$\frac{\Delta \tau}{\tau_n} = \frac{\tau_H - \tau_L}{\tau_n} = \frac{\Delta f}{f_n} = \frac{\Delta \omega}{\omega_n} = \frac{1}{Q}$$

791

792   In this section we generalize the constant-Q framework to the logarithmic discretization of
793 evaluation intervals relative to a given reference scale and base. For a given reference scale τ_0, which
794 could be time, frequency, spatial length, wavenumber, or any other useful metric, we define a logarithmic
795 scale base $G > 1$ and center scale τ_n as

796

797
$$\frac{\tau_n}{\tau_0} = G^{\frac{n}{N}}$$

798

799 where n is the band number and N is the band order, subject to the constraints
800 $n \in \mathbb{Z}, \ N \geq 1$.

801

802   The natural base for both contemporary and quantum computers is base 2, and analysis windows
803 with powers of two are recommended for complex computations at large scales. Many efficient
804 algorithms are based on binary (base two) filter banks. Selecting $G = 2$ yields

805

806
$$\frac{\tau_n}{\tau_0} = 2^{\frac{n}{N}}, \qquad \frac{\tau_H}{\tau_n} = 2^{\frac{1}{2N}}, \qquad \frac{\tau_L}{\tau_n} = 2^{-\frac{1}{2N}}, \qquad \frac{\tau_H \tau_L}{\tau_n^2} = 1$$

807

808
$$Q_N = \left[2^{\frac{1}{2N}} - 2^{-\frac{1}{2N}} \right]^{-1}$$

809
810
811   Note that center and band edge scales attached to a given band n change with the order N, reference
812 scale τ_0, and the reference base G. If the reference scale and base are standardized, all bands are invariant.
813 For example, the concert A pitch standard is fixed at 440 Hz and may be used to tune other instruments
814 anywhere and at any time.

815

816   The next step substantially simplifies the estimation of constant-Q bands with a minimal
817 introduction of a 2% computational error. To the author's knowledge, this is the first time this expression
818 is presented (and he would be most grateful to be informed otherwise). Numerical evaluation shows that:
819

820
$$\lim_{N\to\infty} \frac{Q_N}{Q_1} = \lim_{N\to\infty} \left(G^{\frac{1}{2}} - G^{-\frac{1}{2}} \right) \left(G^{\frac{1}{2N}} - G^{-\frac{1}{2N}} \right)^{-1} \approx N\frac{G-1}{\sqrt{G}\ln(G)} \approx (1.02\,)N \approx N$$

821

822
$$Q_N \approx NQ_1 = N\left[\frac{\sqrt{G}}{G-1} \right]$$

823

824 The center frequencies and band edges, and thus the quality factor, of traditional fractional octave bands
825 are well known and can be readily computed for all the standard bands. The primary value of the
826 expression for Q_N is that it provides a simple, explicit estimate of the relation between the quality factor
827 and the band order, which in turn permits an estimate of the support window duration for a given
828 wavelet in terms of the band order. Numerical inspection shows that for most practical applications and
829 for $G = 2 \approx 10^{\frac{3}{10}}$, even those when N is non integer, we can use the expression

830

831
$$Q_N = \frac{f_n}{\Delta f_n} \approx \sqrt{2}N$$

832

833 to estimate the relationship between the band order and the quality factor.

834

835   Although the center frequency is traditionally defined as the geometric mean of the band edges, the
836 ½ power spectral points at the band edges are only symmetric around the arithmetic mean of the center
837 frequency. The relation between the arithmetic mean $f_{na} = (f_L + f_H)/2$ and the geometric mean $f_{ng} = \sqrt{f_L f_H}$ of the center frequency of fractional binary bands is
838
839

840
$$\frac{f_{na}}{f_{ng}} \cong \sqrt{1 + \frac{1}{8N^2}} \approx 1 + \frac{1}{16N^2}$$

841

842 where the approximation uses the binomial expansion. The arithmetic and geometric center frequencies
843 are close to each other, and for fractional octave bands (N>1) get ever tighter. However, the band edge
844 power levels at the half band width $\Delta f_n/2$ should be considered to be relative to the arithmetic mean
845 rather than the geometric mean. In general practice it is easier to use the arithmetic frequency as f_n, with
846 the understanding that the fractional octave specifications are defined by geometric scaling.

847

848   As an extension of the Inferno framework [1] the nominal duration of the Gabor atom window T_n
849 may be defined as a multiple M_N of the scale as

850
$$T_n(N,n) \overset{\text{def}}{=} M_N \tau_n = M_N \tau_0 G^{\frac{n}{N}}$$

851

852 where the scale multiplier M_N is set by the half power points of the wavelet. Traditional constant-Q
853 frameworks in acoustics and music applications match the 12-tone equal temperament system (N=12) for
854 $G = 2$ or $G = 10^{\frac{3}{10}} \approx 2$ and are consistent with the Renard series recommended in ISO3 for N=1, 3, 6, 12,
855 24.

856

857 **Appendix B. The Gabor Atom**

858   Different disciplines call the same things different names; many of the challenges in present-day
859 data science are often due to divergent lexicon and the diversity of applications specific to each field. The
860 idea of using a windowed sinusoid as a basis function for signal representation was developed in detail
861 in Gabor's [2] landmark paper, where he also introduced the time-frequency uncertainty principle.

862 Gabor's atoms were further developed by Grossman and Morlet [14] and P. Goupillaud et al. [15]
863 (amongst others), who formalized and popularized what we now know as *wavelet* transforms. Mallat [13]
864 presents a lucid overview of the complementary nature of Fourier and wavelet representations in his
865 Wavelet Tour of Signal Processing; the serious student would be wise to consider it required reading.
866
867   The Gabor wavelet is a special case of a wavelet-modulated window ([13] Eqs. 4.60-4.62) and is
868 representative of a bandwidth-limited compressed pulse [12]. For a physical scientist, its most intuitive
869 form is

870
$$\Psi(x) = \frac{1}{[\pi\sigma^2]^{1/4}} exp\left(-\frac{x^2}{2\sigma^2}\right) \exp(i\eta_n x),$$

871
872 representing a sinusoid with time t and scaled angular frequency η_n (or linear space and wavenumber)
873 modulated by Gaussian window with standard deviation σ. Comparison with the canonical expression

874
$$\Psi_n(x) = \frac{1}{(\pi s_n^2)^{1/4}} exp\left\{-\frac{1}{2}\left[\frac{x}{s_n}\right]^2\right\} exp\left\{i\left[\frac{2\pi f_n}{f_s}\right]x\right\}$$

875 shows that the scaled angular frequency and standard deviation are
876

877
$$\eta_n = \frac{2\pi f_n}{f_s}, \quad \sigma = s_n, \quad \sigma\eta = M_N \frac{f}{f_n}$$

878
879 The Fourier transform of the mother wavelet is
880

881
$$\hat{\Psi}(\eta) = [4\pi\sigma^2]^{1/4} exp\left\{-\frac{1}{2}\sigma^2[\eta - \eta_n]^2\right\} = [4\pi s_n^2]^{1/4} exp\left\{-\frac{1}{2}M_N^2\left[\frac{f}{f_n} - 1\right]^2\right\},$$

882 has unit second moment

883
$$\int_{-\infty}^{\infty} \Psi(x)\Psi^*(x)dx = 1 ,$$

884 and it first moment vanishes in the limit
885

886
$$\int_{-\infty}^{\infty} \Psi(t)dt \rightarrow 0 \text{ for } \sigma^2\eta_c^2 \gg 1 .$$

887
888 Another important representation of the Gabor wavelet [27-28] is
889

890
$$\psi = (4\pi\sigma^2)^{-\frac{1}{4}} \Psi$$

891
$$\psi(x) = \frac{1}{[2\pi\sigma^2]^{\frac{1}{2}}} exp\left\{-\frac{x^2}{2\sigma^2}\right\} exp\{i\eta_c x\}$$

892
893 With the advantage that its Fourier transform
894

895
$$\hat{\psi}(\eta) = exp\left\{-\frac{1}{2}\sigma^2[\eta - \eta_c]^2\right\} = exp\left\{-\frac{1}{2}M_N^2\left[\frac{f}{f_n} - 1\right]^2\right\},$$

896
897 has a peak amplitude of unity and yields equal-amplitude filter banks.
898
899   The Inferno framework was developed with the introduction of multiresolution array processing in
900 the field of infrasound. The time duration of an analysis window at a specific period is represented as

901
$$T_n = M_N \, \tau_n.$$

902

903 This time window generally sets the temporal resolution of the resulting data products. In the case of the
904 STFT, the analysis window can be referred to as the window of integration. In other words, the
905 integration window T_n is defined as a multiple M_N of the pseudo period. This window immediately
906 constrains the lowest frequency f_{min} that can be represented and the resolution of a spectral
907 representation,

908
$$f_{min} = \frac{1}{T_n}$$

909

910 The upper bandwidth of the analysis window can be set by the Nyquist frequency, which is half of the
911 sampling frequency of the digital time series. In practice the upper bandwidth is close to one quarter of
912 Nyquist. Although this representation is simple and tidy, it is not particularly informative. A more useful
913 representation of window duration is the number of wavelet oscillations in the window, which can be
914 estimated from the quality factor Q_N of the wave function. As presented in Appendix C, the relation
915 between the scale multiplier M_N and the quality factor can be estimated by the ½ power (-3dB, or half
916 bit) points on the power spectrum,

917
$$M_N = 2\sqrt{ln2} \, Q_N$$

918

919 The wavelet admissibility condition for the for this wavelet is equivalent to the zero mean, or

920

921
$$M_N^2 \gg 1$$

922

923 which is essentially met by the standard bands presented in Table 1. Although traditionally the Nth
924 octave frequencies are represented by the geometric mean of the band edge frequencies (Appendix A),
925 in the evaluation of spectral power losses it is important to use the arithmetic mean for f_n which would
926 be centered in the bandwidth Δf_n in linear frequency space. Since the ratios of the arithmetic and
927 geometric means are constant and set by the band order N, the geometric scaling is still preserved.

928

929 The canonical form for computational evaluation is:

930
$$\Psi_n(x - x') = \frac{1}{\pi^{1/4}} \frac{1}{\sqrt{s_n}} \, exp\left\{-\frac{1}{2}\left[\frac{x-x'}{s_n}\right]^2\right\} exp\left\{iM_N\left[\frac{x-x'}{s_n}\right]\right\}$$

931

932 The second b-type form has a different structure

933
$$\psi_n(x) = \Psi_{x',n}(x)(4\pi)^{-\frac{1}{4}} s_n^{-\frac{1}{2}}$$

934

935
$$\psi_n(x - x') = (2\pi)^{-\frac{1}{2}} s_n^{-1} \, exp\left\{-\frac{1}{2}\left[\frac{x-x'}{s_n}\right]^2\right\} exp\left\{i2\pi \frac{f_n}{f_s}(x - x')\right\}$$

936 applying

937
$$s_n = s_0 \, 2^{\frac{n}{N}},$$

938 yields

939
$$\psi_n(x - x') = (\pi \, 2s_0^2)^{-\frac{1}{2}} [s_n]^{-1} \, exp\left\{-\frac{1}{2s_0^2}\left[\frac{x-x'}{s_n}\right]^2\right\} exp\left\{i\frac{M_N}{s_0}\left[\frac{x-x'}{s_n}\right]\right\}$$

940 which has the form

941
$$\psi_N(\mu) = \frac{1}{\sqrt{\pi b}} \, exp\left\{-\frac{\mu^2}{b}\right\} exp\left\{i\frac{M_N}{s_0}\mu\right\}$$

942
$$\psi_n(\mu) = \frac{1}{s_n}\psi_N\left(\frac{\mu - \mu'}{s_n}\right)$$

943   with

944
$$s_n = \frac{s_n}{s_0} = 2^{\frac{n}{N}}, \ n \geq 0, \qquad s_0 = M_N \frac{f_s\tau_0}{2\pi}$$

945
$$b = 2s_0^2 = 2\left[M_N \frac{f_s\tau_0}{2\pi}\right]^2$$

946   Note that since

947
$$b = 8ln2\left(\frac{f_s}{\Delta\omega_0}\right)^2$$

948   the "bandwidth" b is inversely proportional to the actual bandwidth of the highest frequency.

949

950   **Appendix C. The Q of the Quantum Wavelet**
951
952   The power spectral density of the Gabor wavelet is:

953
$$\hat{\Psi}^2{}_n(f) = [4\pi s_n^2]^{1/2} \, exp\left\{-M_N^2\left[\frac{f - f_n}{f_n}\right]^2\right\},$$

954

955
$$\frac{\hat{\Psi}^2{}_{u,n}(f_n \pm \Delta f_n/2)}{\hat{\Psi}^2{}_{u,n}(f_n)} = exp\left\{-M_N^2\left[\frac{\Delta f_n}{2f_n}\right]^2\right\} = exp\left\{-\left[\frac{M_N}{2Q_N}\right]^2\right\} = \frac{1}{Y}$$

956
957   Where Y is the fractional power loss. There exist various definitions of the quality factor of a system. This
958   paper defines Q_N by 1/2 of the spectral power relative to the peak spectral power, where $Y = 2$.
959   Therefore, for the Gabor wavelet,
960
961
$$M_N = 2\sqrt{ln2}\, Q_N$$

962
963   Consider the decay of the spectrum relative with distance δ from the peak frequency
964

965
$$\frac{\hat{\Psi}^2{}_{u,n}(f_n + \delta\Delta f_n/2)}{\hat{\Psi}^2{}_{u,n}(f_n)} = exp\left\{-\left[\frac{\delta M_N}{2Q_N}\right]^2\right\} = exp\left\{-\left[\delta\sqrt{ln2}\right]^2\right\} = 2^{-\delta^2}$$

966
967   The loss in dBs and binary bits can be expressed as
968
969
$$dB = 10*log_{10}(2^{-\delta^2}) = -\delta^2 10*log_{10}(2) \approx -3\delta^2$$

970
$$bR = \frac{1}{2}log_2(2^{-\delta^2}) = \frac{-\delta^2}{2}$$

971
972   There is a loss of 3dB, 12dB, 27dB, and 48dB, and a binary power loss of ½, 2, 4.5, and 8 fbits, for integer
973   multiples of the bandedge $\delta = 1, 2, 3, 4$, respectively.
974   It is worth considering an alternate definition for the quality factor of an oscillator. Consider the time
975   required for the amplitude to drop to 1/e of its peak value. In the case of the Quantum wavelet this is set

976   by the Gaussian envelope, and this particular definition is best suited for the real part of the wavelet
977   which is symmetric about the origin. By applying this definition,
978

979
$$exp\left\{-\frac{1}{2}\left[\frac{x}{s_n}\right]^2\right\} = exp\left\{-\frac{1}{2}\left[\frac{f_s\tau_e}{s_n}\right]^2\right\} = exp\left\{-\frac{1}{2}\left[\frac{\omega_n\tau_e}{M_N}\right]^2\right\} = exp\{-1\}$$

980

981
$$\tau_e = \frac{\sqrt{2}}{\pi}\frac{T_n}{2} \approx 0.45\frac{T_n}{2}$$

982
983   Since the wavelet is symmetric, this states that the portion of the wavelet contained within $2\tau_e$ of the
984   window has an amplitude above 1/e of the peak. The quality factor associated with this type of oscillator
985   is

986
$$Q_e = \frac{\omega_n\tau_e}{2} = \frac{M_N}{\sqrt{2}}$$

987
988   and comparison with the half power point quality factor shows
989

990
$$Q_e = \sqrt{2ln2}\ Q_N \approx 1.1774\ Q_N$$

991
992   and they are sufficiently close to each other to be equivalent for descriptive purposes. The time duration
993   of the quantum wavelet is defined by
994

995
$$T_n = M_N\ \tau_n = 2\sqrt{ln2}\ Q_N\tau_n$$

996
997   where $Q_N \approx Q_e$ can be interpreted as the number of oscillations in a little less than half of the total
998   window T_n with amplitude above 1/e of the maximum amplitude. The remaining half of the window is
999   useful to allow the wavelet to settle down and meet the desirable condition of a vanishing first moment.
1000   Practical implementations of Gabor wavelets and their variants often have to make some
1001   compromises in the application of the wavelet duration T_n, in particular if the window is required to be
1002   a power of two. Direct integration of the wavelet power over the window T_n shows that it contains
1003   99.999% of all the power. Integration over $2\tau_e$ will be insufficient. However, there exists a third quality
1004   factor defined by
1005

1006
$$exp\left\{-\frac{1}{2}\left[\frac{\omega_n\tau_\pi}{M_N}\right]^2\right\} = exp\{-\pi\}$$

1007   where

1008
$$Q_\pi = \frac{\omega_n\tau_\pi}{2}$$
1009
$$Q_\pi = \sqrt{\pi}\ Q_e \approx 1.7724\ Q_e$$
1010

1011
$$\tau_\pi = \sqrt{\pi}\ \tau_e = \sqrt{\frac{2}{\pi}}\frac{T_n}{2} \approx 0.7978\frac{T_n}{2}$$

1012
1013   In other words, $2\tau_\pi$ encompasses ~80% of the window, and integration of the wavelet power over $2\tau_\pi$
1014   returns 99.96% of the total power. Therefore $2\tau_\pi = 0.8T_n$ may be a reasonable lower bound for the
1015   wavelet duration. This is further considered in the next Appendix.
1016
1017   **Appendix D. The Gabor Box**
1018

1019   Gabor introduced the time-frequency uncertainty principle in his landmark paper [2]. It is not
1020   possible to observe for all time and reach zero frequency. It is also impossible to sample infinitely fast
1021   and reach infinite frequency. All observations require a restriction in the observation time and the
1022   observation rate, and this places hard limits on the observable bandwidth of a process. The fundamental
1023   discretization interval scale invokes the Gabor uncertainty principle, which states the time and period of
1024   a signal cannot be known exactly but can be contained inside the box defined by the temporal and
1025   frequency variance of the probability distribution of the wave function.
1026   This section follows the generalized mathematical formalism of [13], Section 2.3.2, Uncertainty
1027   Principle. As in [13] and [7] the Fourier Transform pair used in this work is

1028
$$\hat{f}(\omega) = \int_{-\infty}^{\infty} f(t)e^{-j\omega t}\, dt$$

1029
$$f(t) = \frac{1}{2\pi}\int_{-\infty}^{\infty} \hat{f}(\omega)e^{j\omega t}\, d\omega \ ,$$

1030   where $\hat{f}(\omega)$ and $f(t)$ may be complex. The Parseval-Plancherel identity asserts that
1031

1032
$$\|f\|^2 = \int_{-\infty}^{\infty} |f(t)|^2\, dt = \frac{1}{2\pi}\int_{-\infty}^{\infty} \left|\hat{f}(\omega)\right|^2 d\omega = \frac{1}{2\pi}\left\|\hat{f}\right\|^2$$

1033
1034   where
1035
$$|f|^2 = f \cdot f^*$$

1036
1037   and the asterisk denotes complex conjugation. A related identity the for product is routinely used in
1038   Fourier and Wavelet analyses and the application of filter banks.
1039

1040
$$\int_{-\infty}^{\infty} f(t)g^*(t)\, dt = \frac{1}{2\pi}\int_{-\infty}^{\infty} \hat{f}(\omega)\hat{g}^*(\omega)\, d\omega$$

1041
1042   The Gabor uncertainty principle constrains uncertainty to Gabor box defined by the variance in time
1043   and frequency. It is equivalent to the Heisenberg uncertainty principle for position and momentum
1044   extended to time and frequency, or space and wavenumber. Let a one-dimensional signal of interest be
1045   represented by a wave function $f(t)$. The probability density that a signal can be localized in time at a
1046   given time t is

1047
$$\frac{|f(t)|^2}{\|f\|^2} = \frac{2\pi|f(t)|^2}{\|\hat{f}\|^2},$$

1048   and the probability density that its angular frequency is ω is

1049
$$\frac{|\hat{f}(\omega)|^2}{\|\hat{f}\|^2} = \frac{|\hat{f}(\omega)|^2}{2\pi\|f\|^2}.$$

1050   The variance in the time localization of the signal as

1051
$$\sigma_t^2 = \frac{1}{\|f\|^2}\int_{-\infty}^{\infty} (t-u)^2\, |f(t)|^2\, dt.$$

1052   and the variance in the frequency localization of the signal as
1053

1054
$$\sigma_\omega^2 = \frac{1}{\|\hat{f}\|^2}\int_{-\infty}^{\infty} (\omega-\xi)^2\, |\hat{f}(\omega)|^2\, d\omega.$$

1055

1056   Reference [13] uses these expressions to rederive the Heisenberg-Gabor uncertainty principle, which
1057   states that the temporal and angular frequency variance satisfy:

1058
$$\sigma_t^2 \sigma_\omega^2 \geq \frac{1}{4}$$

1059   In the special case of the Gabor-Morlet wavelet and its Quantum spawn, where the wave function
1060   is symmetric and centered around the time-shift u and the spectrum is symmetric relative to the peak
1061   frequency ω_n, the variance for the time and frequency distribution of the signal wave function can be
1062   readily evaluated.

1063
$$\sigma_t^2 = \frac{1}{\|\psi_H\|^2} \int_{-\infty}^{\infty} (t-u)^2 \, |\psi_H(t-u)|^2 \, dt = \frac{1}{2} s_n^2$$

1064
$$\sigma_{\omega n}^2 = \frac{1}{\|\hat{\psi}_H\|^2} \int_{-\infty}^{\infty} (\omega - \omega_n)^2 \, \left|\hat{\psi}_H(\omega - \omega_n)\right|^2 \, d\omega = \frac{1}{2} s_n^{-2}$$

1065

1066   and the Gabor box defined by the variance is minimal,

1067
$$\sigma_t^2 \sigma_{\omega n}^2 = \frac{1}{4},$$

1068   which is another reason for this wavelet's popularity.
1069   Consider the standard deviation for time integrated over the scaled window ϵT_n
1070

1071
$$\sigma_t^2(\epsilon) = \frac{1}{\|\psi_H\|^2} \int_{u-\frac{\epsilon T_n}{2}}^{u+\frac{\epsilon T_n}{2}} (t-u)^2 \, |\psi_H(t-u)|^2 \, dt = \frac{1}{\sqrt{\pi}} \left[\frac{M_N}{\omega_n}\right]^2 \int_{-\epsilon\pi}^{\epsilon\pi} x^2 \, e^{-x^2} \, dx$$

1072

1073
$$\int_{-a}^{a} x^2 \, e^{-x^2} \, dx = \frac{\sqrt{\pi}}{2}\left[erf(a) - \frac{2}{\sqrt{\pi}} a \, e^{-a^2}\right]$$

1074
1075   For $\epsilon \geq \frac{3}{2\pi}$

1076
$$\sigma_t^2(\epsilon) \cong \frac{1}{2} s_n^2 \, erf(\epsilon\pi)$$

1077
1078   For $\epsilon = [1.0, 0.8, 0.45]$

1079
$$\sigma_t^2(\epsilon) \cong \frac{1}{2} s_n^2 \, [0.9999, 0.9996, 0.9544\,]$$

1080   where ϵ corresponds to integration over T_n, $2\tau_\pi \approx 0.8 T_n$, and $2\tau_e \approx 0.45 T_n$, corresponding to the full
1081   window, the decay time associated with Q_π, and the e-folding time associated with Q_e, respectively
1082   (Appendix D).
1083   Next, consider the standard deviation for time integrated over the scaled window ϵT_n
1084

1085
$$\sigma_{\omega n}^2(\delta) = \frac{1}{\|\hat{\psi}_H\|^2} \int_{\omega_n - \frac{\delta\Delta\omega_n}{2}}^{\omega_n + \frac{\delta\Delta\omega_n}{2}} (\omega - \omega_n)^2 \, \left|\hat{\psi}_H(\omega - \omega_n)\right|^2 \, d\omega = = \frac{1}{\sqrt{\pi}} \left[\frac{M_N}{\omega_n}\right]^{-2} \int_{-\delta\sqrt{\ln 2}}^{\delta\sqrt{\ln 2}} x^2 \, e^{-x^2} \, dx$$

1086

1087
$$\sigma_{\omega_n}^2(\delta) \cong \frac{1}{2}s_n^{-2}\left[erf\left(\delta\sqrt{ln2}\right) - \frac{2}{\sqrt{\pi}}\left(\delta\sqrt{ln2}\right)2^{-\delta^2}\right]$$

1088

1089   For $\delta = [1, 2, 3, 4]$

1090
$$\sigma_{\omega_n}^2(\delta) \cong \frac{1}{2}s_n^{-2}\,[0.2912, 0.8640, 0.9941, 0.9999]$$

1091

1092   where δ corresponds to integration over $\Delta\omega_n, 2\Delta\omega_n, 3\Delta\omega_n, and\ 4\Delta\omega_n$, respectively. These results show
1093   that the Gabor box can be well approximated (>99% of the variance) by a window of duration $2\tau_\pi =$
1094 $0.8T_n$ and a bandwidth of $3\Delta\omega_n$, and over 99.99% of the variance is contained by a Gabor box of
1095   dimensions T_n, $4\Delta\omega_n$. In other words, third octave bands will contain over 99% of the variance within its
1096   octave and within 80% of the full window T_n.

1097

1098   **Appendix E. The Gabor Family**

1099

1100   A few variations of the Gabor-Morlet wavelet are available in present-day computing environments.
1101   One of the more familiar forms of the mother wavelet used in modern computations [27-28] is

1102
$$\psi(\mu) = \frac{1}{\sqrt{\pi b}}\ exp\left\{-\frac{\mu^2}{b}\right\}exp\{i2\pi\bar{f}_b\,\mu\}$$

1103
$$\psi_{\mu',n}(t) = \frac{1}{s_n}\psi\left(\frac{\mu-\mu'}{s_n}\right)$$

1104   This form is found in the Matlab "cmor" function as well as the Python Pywavelets [29] "cmorB-C"
1105   function with $C = \bar{f}_b$. The term b is referred to as the "bandwidth parameter" of the wavelet. The
1106   Quantum wavelet has the equivalence

1107
$$s_n = 2^{\frac{n}{N}},\ \ n \geq 0,$$

1108
$$\tau_n = \tau_0 s_n = \frac{1}{f_0}s_n$$

1109
$$b = 2\left[M_N\frac{f_s\tau_0}{2\pi}\right]^2$$

1110
$$C = \bar{f}_b = \frac{f_0}{f_s} = \frac{1}{f_s\tau_0}$$

1111   Where f_0, the highest center frequency, is used as the starting point. The scaled wavelet duration is $M_N\frac{f_s}{f_n}$
1112   and can be rounded to approximate the number of points for each scale.

1113   Foster [30] expresses the abbreviated Morlet wavelet as
1114

1115
$$F(z) = e^{iz-cz^2} = exp\left\{i\omega_n t - \frac{1}{2M_N^2}\omega_n^2 t^2\right\}$$

1116

1117   So that $z = \omega_n t$ and now $c = \frac{1}{2M_N^2}$ is inversely proportional to the Q of the wave function. The beauty of
1118   Foster's approach is that it can be used for unevenly sampled data. A modernization of this algorithm
1119   can be found at [31].

1120

1121   **Appendix F. The Analytic Function for the GT Blast Pulse**

1122   The reconstruction coefficients of the complex Morlet CWT return the imaginary part of the
1123   analytic signal. The complex analytic signal corresponding to the real signal $g(\hat{t})$ is

1124
$$g_{\mathbb{C}}(\hat{t}) = g(\hat{t}) + j\,\mathcal{H}[g(\hat{t})]$$

1125   Where $\mathcal{H}$ denotes the Hilbert transform, a recurrent topic in wave propagation as reflection introduces
1126   phase shifts that are often modeled as Hilbert transforms of the original signal [32]. For example, some
1127   of the U-shaped infrasound waveforms associated with thermospheric returns resemble the Hilbert
1128   transform of an explosion pulse [3]. The Hilbert transform is also useful for estimating instantaneous
1129   frequency and in the computation of the Hilbert-Huang transform [33].

1130   Let $\boldsymbol{g(\hat{t})}$ represent the GT pulse,

1131
$$g(\hat{t}) = (1 - \hat{t}), \quad 0 \le \hat{t} \le 1$$

1132
$$g(\hat{t}) = \frac{1}{6}(1 - \hat{t})(1 + \sqrt{6} - \hat{t})^2, \quad 1 < \hat{t} \le 1 + \sqrt{6} \ .$$

1133   The Hilbert transform of the canonical GT blast pulse is rather unwieldy, but can be evaluated from

1134
$$g_{\mathcal{H}}(\hat{t}) = \mathcal{H}[g(\hat{t})] = \mathcal{P}\,\frac{1}{\pi}\int_{-\infty}^{\infty}\frac{g(x)}{t - x}dx$$

1135   Where the $\mathcal{P}$ in front of the integral denotes the Chaucy principal value. Multiple integration by parts
1136   over the interval of the GT pulse yields

1137
$$g_{\mathcal{H}}(\hat{t}) = \frac{1}{\pi}[1 + (1 - \hat{t})ln(-\hat{t}) - (1 - \hat{t})ln(1 - \hat{t})], \qquad 0 \le \tau \le 1$$

1138
$$g_{\mathcal{H}}(\hat{t}) = \frac{1}{6\pi}\frac{(a - 1)}{6}[a(2a + 5) - 1 + 6\hat{t}^2 - 3\hat{t}(1 + 3a)]$$

1139
$$+ \frac{1}{6\pi}[(\hat{t} - 1)(a - \hat{t})^2][ln(a - \hat{t}) - ln(1 - \hat{t})], \quad 1 < \tau \le a = 1 + \sqrt{6}\,.$$

1140   Since

1141
$$\lim_{x \to 0} x\,ln(x) = 0\,, \qquad \lim_{x \to 0} x^2\,ln(x) = 0$$

1142   The solutions are well behaved near the zero crossings. However, there are some issues in this solution.
1143   First, there are the two troublesome implicitly complex terms. The first is

1144
$$ln(-\hat{t}) = ln(\hat{t}) + j\pi, \qquad 0 \le \tau \le 1$$

1145   where $ln(\hat{t})$ tends to negative infinity at $\hat{t} = 0$. The second tricky term is

1146
$$ln(1 - \hat{t}) = ln(\hat{t} - 1) + j\pi, \qquad 1 < \tau \le 1 + \sqrt{6}$$

1147   The complex terms are awkward; fortunately, multiplication and division by zero can be readily avoided
1148   numerically by adding the smallest floating point value (float epsilon) to arguments in logarithmic
1149   computations so it is possible to evaluate the real part of the solution. Another inconvenience is the
1150   discontinuity in $g_{\mathcal{H}}$ and its slope as $\hat{t} \to 1$. Rewriting the first term as

1151
$$g_{\mathcal{H}}(\hat{t})_{\hat{t}<1} = \frac{1}{\pi}[1 + (1 - \hat{t})ln(\hat{t}) - (1 - \hat{t})ln(1 - \hat{t})] + j(1 - \hat{t}), \qquad \hat{t} \to 1\,from\,below$$

1152
$$g_{\mathcal{H}}(\hat{t} \to 1) = \frac{1}{\pi}$$

1153   Evaluating the second term yields

1154
$$g_{\mathcal{H}}(\hat{\tau} = 1) = \frac{1}{\pi}\frac{\sqrt{2}}{\sqrt{3}} = \frac{1}{\pi}\left[1 - \frac{\sqrt{3} - \sqrt{2}}{\sqrt{3}}\right], \qquad \hat{\tau} \to 1 \; from \; above$$

1155   These deficiencies are suboptimal, and not altogether surprising given that the waveform [7] did not
1156   design integrability into the GT pulse. Fortunately, these inadequacies are deemed computationally
1157   irrelevant by using the numerical convolution provided by the SciPy [25] signal.hilbert, which returns
1158   the analytic function for an input real signal. The comparison between the unfiltered synthetic theoretical
1159   analytic signals, the CWT reconstruction, and the numerical Hilbert transform are presented in the
1160   figures in the main text.

1161

1162   **Funding:** This material is based upon work supported in part by the Department of Energy National Nuclear
1163   Security Administration under Award Numbers DE-XXXX and the Air Force Research Laboratory under agreement
1164   FAXXXX.

1173   **Acknowledgments:** The author is thankful to two anonymous reviewers who helped improve the accessibility of
1174   the document. A. Christe, B. Williams, S. Takazawa and J. Tobin helped review various drafts of the document. Many
1175   thanks for E. Lam, S. Leung, J. Carlo, A. Smith, A. Rangarajan, J. Zeineddine for providing valuable context.

1176   **Conflicts of Interest:** The author declares no conflict of interest. The funders had no role in the design of the study;
1177   in the collection, analyses, or interpretation of data; in the writing of the manuscript, or in the decision to publish the
1178   results.

References

1180   1.   Garcés, M. A. On Infrasound Standards, Part 1. Time, frequency, and Energy scaling. Inframatics, 2013, 2, 13-
1181   35, doi:10.4236/inframatics.2013.22002.
1182   2.   Gabor, D. Theory of Communication, Part 3, Electrical Engineers, 1946, Vol. 93, No. 26, pp. 445-457.
1183   3.   Vergoz, J.; LePichon, A; Millet, C. The Antares explosion observed by the USArray: an unprecedented collection
1184   of infrasound phases recorded from the same event. In Infrasound Monitoring for Atmospheric Studies, 2nd
1185   ed.; Le Pichon, A.; Blanc, E.; Hauchecorne, A. Eds; Springer Nature: Switzerland, 2019; DOI 10.1007/978-3-319-
1186   75140_5, p. 349-386.
1187   4.   Mialle, P.; Brown, D.; Arora, N. Advances in operational processing at the international data center. In
1188   Infrasound Monitoring for Atmospheric Studies, 2nd ed.; Le Pichon, A.; Blanc, E.; Hauchecorne, A. Eds;
1189   Springer Nature: Switzerland, 2019; DOI 10.1007/978-3-319-75140_5, p. 273-345.
1190   5.   Yu, Q.; Yao, Y.; Wang, L.; Tang, H.; Dang, J.; Tan, K. C. Robust Environmental Sound Recognition with Sparse
1191   Key-point Encoding and Efficient Multi-spike Learning. arXiv:1902.01094, 2019
1192   6.   Severa, W.; Vineyard, C. M.; Rellana, R., Verzl, S., Almone, J. B. Training Deep Neural Networks for Binary
1193   Communication with the Whetstone Networks, Nat Mach Intell, 2019, 1, 86-94, https://doi.org/10.1038/s42256-
1194   018-0015-y
1195   7.   Garcés, M. A. Explosion Source Models. In Infrasound Monitoring for Atmospheric Studies, 2nd ed.; Le Pichon,
1196   A.; Blanc, E.; Hauchecorne, A. Eds; Springer Nature: Switzerland, 2019; DOI 10.1007/978-3-319-75140_5, p. 273-
1197   345.

8. Pacenak, Z.; Kleissl, J.; Lam E. "Detection of a Surface Detonated Nuclear Weapon using a Photovoltaic Rich Microgrid", IEEE Power and Energy Society General Meeting, San Diego, CA, 1 Aug 2018.

9. Cai, Y.; Lam, E.; Howlett, T.; Cai, A. Spatiotemporal Analysis of 'Jello Effect' in Drone Videos, 10th International Conference on Applied Human Factors and Ergonomics, Washington D.C., USA, 26 July 2019.

10. Elliot, D.; Martino, E.; Otero, C. E.; Smith, A.; Peter, A.; Luchterhand, B.; Lam, E.; Leung, S. Cyber-Physical Analytics: Environmental Sound Classification at the Edge. IEEE World Forum on the Internet of Things 2020, Edge and Fog Computing Paper 1205, New Orleans, 5-9 April 2020.

11. Shannon, C. E., The Mathematical Theory of Communication. Urbana, IL, University of Illinois Press, 1998 [1949].

12. Berg, N. J.; Pellegrino, J. M. Acousto-optic Signal Processing: Theory and Implementation. Marcel Dekker, NY, 1996, ISBN 0-8247-8925-3.

13. Mallat, S., A Wavelet Tour of Signal Processing: The Sparse Way, Academic Press, 1998, 3rd edn. 2009.

14. Grossmann, A.; Morlet, J. Decomposition of Hardy Functions into Square Integrable Wavelets of Constant Shape. Soc. Int. Am. Math. (SIAM), J. Math. Analys. 1984, Vol. 15, pp. 723-736.

15. Goupillaud, P.; Grossmann, A.; Morlet, J. Cycle-octave and Related Transforms in Seismic Signal Analysis. Geoexploration 1984, Vol 23, Issue 1, 1984, Pages 85-102, ISSN 0016-7142, https://doi.org/10.1016/0016-7142(84)90025-5.

16. Sheu, Y.-L.; Hsu, L.-Y.; Wu, H.-T.; Li, P.-C.; Chu, S.-I. A New Time-Frequency Method to Reveal Quantum Dynamics of Atomic Hydrogen in Intense Laser Pulses: Synchrosqueezing Transform, AIP Advances 2014, 4, 117138; https://doi.org/10.1063/1.4903164

17. Ashmead,J. Morlet Wavelets in Quantum Mechanics. Quanta 2012, 1(1), 58-70; doi:https://doi.org/10.12743/quanta.v1i1.5

18. Canolty, R. T.; Womelsdorf, T. Multiscale Adaptive Gabor Expansion (MAGE): Improved Detection of Transient Oscillatory Burst Amplitude and Phase, bioRxiv 369116, 2019; doi: https://doi.org/10.1101/369116

19. Shi, Y.; Xian-Da Zhang, X.-D. A Gabor Atom Network for Signal Classification with Application in Radar Target Recognition. IEEE Transactions on Signal Processing 2001, vol. 49, no. 12, pp. 2994-3004, doi: 10.1109/78.969508.

20. Li, T; Zhou, M. ECG Classification Using Wavelet Packet Entropy and Random Forests. Entropy 2016, 18, 285;

21. Torrence, C.; Compo, G. P. A Practical Guide to Wavelet Analysis. Bull. Amer. Meteor. Soc. 1998, 79, 61–78, https://doi.org/10.1175/1520-0477(1998)079<0061:APGTWA>2.0.CO;2

22. Farge, M., Wavelet Transforms and their Applications to Turbulence. Annual Review of Fluid Mech. 1992, 24:1, 395-458, doi: 10.1146/annurev.fl.24.010192.002143.

23. Lebedeva E.A.; Postnikov E.B. On Alternative Wavelet Reconstruction Formula: A Case Study of Approximate Wavelets. R Soc Open Sci. 2014; 1(2):140124; doi:10.1098/rsos.140124

24. Bishop, M., http://mark-bishop.net/signals/CWTReconstructionFactors.pdf, Last modified 2018-07-29.

25. Li, T; Zhou, M. ECG Classification Using Wavelet Packet Entropy and Random Forests. Entropy 2016, 18, 285; doi:10.3390/e18080285.

26. Virtanen, P.; Gommers, R.; Oliphant, T.E. *et al*. SciPy 1.0: fundamental algorithms for scientific computing in Python. Nat Methods 2020, 17, 261–272. https://doi.org/10.1038/s41592-019-0686-2

27. Mallat, S., Group Invariant Scattering. Comm. Pure Appl. Math. 2012, 65(10):1331–1398.

28. Mallat, S.; Zhang, S.; Rochette, G.. Phase Harmonic Correlations and Convolutional Neural Networks. IMA J. of Information and Inference 2019; https://arxiv.org/abs/1810.12136

29. Lee, G. R.; Gommers, R.; Wasilewski, F.; Wohlfahrt, K.; O'Leary, A.. PyWavelets: A Python Package for Wavelet Analysis. Journal of Open Source Software 2019, 4(36), 1237, https://doi.org/10.21105/joss.01237.

30. Foster, G. Wavelets for Period Analysis of Unevenly Sampled Time Series. Astronomical J. 1996, Vol. 112(4), pp.1709-1729.

31. Takazawa, S. Weighted Wavelet Z-Transform repo. https://bitbucket.org/redvoxhi/libwwz/src/master/, v1.0.0. 2020.

32. Brekhovskikh, L. M.; Godin, O. A. Acoustics of Layered Media I, Sections 5.2 and 5.3, Second Edition, Springer-Verlag, New York, 1998.

33. Huang, N. E.; Z. Wu, Z. A Review on Hilbert-Huang Transform: Method and its Applications to Geophysical Studies. Rev. Geophys. 2008, 46, RG2006, doi:10.1029/2007RG000228

1249